UNIVERSITY OF ICELAND

B.S. Thesis

in Geology

The effect of microlite crystallization on melt compositions and derived magma temperatures in the 2021 and 2022 Fagradalsfjall eruptions

Alexandra K. Hafsteinsdóttir

Advisor: Enikő Bali

February 2024

FACULTY OF EARTH SCIENCES

The effect of microlite crystallization on melt compositions and derived magma temperatures in the 2021 and 2022 Fagradalsfjall eruptions

Alexandra K.Hafsteinsdóttir

Thesis submitted in partial fulfillment of a
Baccalaureus Scientiarum degree in Geology

Advisor
Enikő Bali

Faculty of Earth Sciences
School of Engineering and Natural Sciences
University of Iceland
Reykjavik, February 2024

The effect of microlite crystallization on melt compositions and derived magma temperatures in the 2021 and 2022 Fagradalsfjall eruptions

10 ECTS
Thesis submitted in partial fulfillment of a *B.S.* degree in Geology.

Faculty of Earth Sciences
School of Engineering and Natural Sciences
University of Iceland
Askja, Sturlugata 7
101 Reykjavík
Iceland

Telephone: 525 4000

Bibliographic information:
Alexandra K. Hafsteinsdóttir, 2023, *The effect of microlite crystallization on melt compositions and derived magma temperatures in the 2021 and 2022 Fagradalsfjall eruptions*, B.S. thesis, Faculty of Earth Sciences, University of Iceland, 50 pp.

Abstract

The aim of this study was to examine how microlite crystallization influences melt compositions and derived magma temperatures in the 2021 and 2022 Fagradalsfjall eruptions. The 2021 and 2022 Fagradalsfjall products contained basaltic glass, plagioclase, olivine, clinopyroxene and traces of Cr-spinel. The plagioclase was generally euhedral and elongated, the microlites had a length of up to 100 μm, microphenocrysts were up to 500 μm, and macrocrysts were larger than 500 μm, in length. The olivine and clinopyroxene were generally euhedral and isometric, the microlites were up to 70 μm, microphenocrysts up to 500 μm, and macrocrysts were larger than 500 μm in diameter. In 2021, the tephra groundmass (excluding microphenocrysts and macrocrysts) was 90% glass and 10% microlites, where the microlite cargo was dominated by plagioclase. The groundmass in the naturally cooled lava was 64% glass and 36% minerals. In 2022, the tephra groundmass was 84% glass and 16% minerals, whereas the lava groundmass was 78.2% glass and 21.8% minerals. The 2021 tephra is more primitive than the 2021 lava, with the tephra glass containing an average of 8.37% MgO while the lava glass had an average of 6.79% MgO content. The 2022 tephra glass contains an average of 7.56% MgO, while the lava glass had an average of 7.18% MgO. Microlite compositions within the lava samples were added back to the lava glass compositions, yielding a recalculated melt composition which represents the melt before microlite crystallization. The recalculated melt for 2021 contained 9.17% MgO and for 2022 it contained 7.66% MgO. There was a significant difference between calculated temperatures for the 2021 melt compositions. The lava glass returned a temperature of 1160°C, the tephra glass 1202°C and the recalculated melt 1243°C, ± 26°C. The temperature values therefore increased significantly as the melt became more primitive. This is due to the large amount of microlites that crystallized between tephra (10% microlites) and lava (36% microlites) samples, due to prolonged residence of the lava flow on the surface before sampling. There was no significant difference between calculated temperatures for the 2022 melt compositions. The lava glass yielded a temperature value of 1157°C, the tephra glass 1172°C and the recalculated melt 1170°C, ± 26°C. This is likely because little to no microlite crystallization occurred between tephra and lava as the lava was sampled within a day of it emerging from the vent.

Útdráttur

Í þessu verkefni voru áhrif kristöllunar örkristalla á efnasamsetningu bráðar og reiknaðs hitastigs kviku í eldgosunum í Fagradalsfjalli árin 2021 og 2022 skoðuð. Í báðum gosum innihéldu gosefnin basaltgler, plagíóklas, ólivín, klínópýroxen og Cr-spínil. Plagíóklas var yfirleitt ílangt, lengd örkristalla var allt að 100 μm, smádílar allt að 500 μm og stórdílar stærri en 500 μm. Ólivín og klínópýroxen voru yfirleitt jafnhliða/vellaga, örkristallarnir voru allt að 70 μm, smádílarnir allt að 500 μm og stórdílarnir stærri en 500 μm í þvermál. Í gosinu 2021 var grunnmassi gjóskunnar (fyrir utan smádíla og stórdíla) 90% gler og 10% örkristallar, þar af meirihlutinn plagíóklas. Grunnmassinn í hrauninu var 64% gler og 36% örkristallar. Í gosinu 2022 var grunnmassi gjóskunnar 84% gler og 16% örkristallar, á meðan grunnmassi hraunsins var 78.2% gler og 21.8% örkristallar. Gjóskan frá 2021 var frumstæðari en hraunið frá sama ári, þar sem gler gjóskunnar innihélt að meðaltali 8.37% MgO á meðan gler hraunsins innihélt 6.79% MgO. Gjóskan frá 2022 innihélt 7.56% MgO á meðan hraunið frá sama ári innihélt 7.18% MgO. Efnasamsetningu örkristalla í hraununum var bætt við efnasamsetningu glersins í hrauninu til að fá samsetningu kvikunnar fyrir kristöllun örkristalla. Endurreiknaða kvikan frá 2021 innihélt 9.17% MgO en 7.66% MgO í gosinu 2022. Það var talsverður munur á reiknuðu hitastigi kvikunnar í 2021 gosinu. Efnasamsetning hraunsins gaf hitastigið 1160°C, samsetning gjóskunnar gaf 1202°C og samsetning endurreiknuðu kvikunnar gaf 1243°C ± 26°C. Reiknað hitastig hækkaði því talsvert eftir því sem kvikan varð frumstæðari, sem má rekja til mikillar kristöllunar örkristalla í hrauninu frá storknun gjóskunnar (10% örkristallar) og þar til hraunið (36% örkristallar) storknaði vegna lengri dvalar þess á yfirborði fyrir sýnatöku. Það var lítill munur á reiknuðu hitastigi kvikunnar í 2022 gosinu. Efnasamsetning hraunsins gaf hitastigið 1157°C, samsetning gjóskunnar gaf 1172°C og samsetning endurreiknuðu kvikunnar gaf 1170°C ± 26°C. Þetta má rekja til lítillar kristöllunar örkristalla milli storknunar gjósku og hrauns, þar sem að hraunsýnin voru tekin aðeins degi eftir að hraunið kom til yfirborðs.

Dedication

Fyrir ömmu Svanhvíti, sem vakir yfir mér.

For my grandmother, Svanhvít, who watches over me.

Table of Contents

List of Figures

List of Tables

Abbreviations

Ab = Albite

An = Anorthite

BSE = Back scattered electron

Cpx = Clinopyroxene

Di = Diopside

EDS = Energy Dispersive Spectroscopy

En = Enstatite

EPMA = Electron Probe Micro-Analyzer

Fa = Fayalite

Fo = Forsterite

Kd = Fe-Mg exchange coefficient

MAR = Mid-Atlantic Ridge

Mpc = Microphenocryst

Ol = Olivine

OPAM = Olivine-Plagioclase-Augite-Melt

Or = Orthoclase

Ox = Oxide

Plag = Plagioclase

RP = Reykjanes Peninsula

RR = Reykjanes Ridge

SEM = Scanning Electron Microscopy

Wo = Wollastonite

Wt% = Weight percentage

Acknowledgements

First and foremost, I would like to thank my supervisor, Enikő Bali, for providing me with this interesting topic, and for her time, guidance, honesty, and patience throughout the research and writing process. She is very much a professional in her field and I will be forever grateful for having her as my supervisor and for getting the opportunity to learn from her.

Secondly, I would like to thank Alberto Caracciolo for his help in interpreting my data using the various methods used in this thesis, especially the ImageJ software. I would also like to thank him for providing me with additional data from his own studies which helped with my discussions.

Thirdly, I would like to thank Guðmundur Heiðar Guðfinnsson for his time, help and guidance in microprobe analyses, and for reading over the abstracts and providing me with the correct Icelandic wordings.

Finally, I would like to thank my family and friends for keeping me relatively sane throughout this process. Their endless support and belief in me are what keep me going.

1 Introduction

On March 19th, a fissure opened in the Fagradalsfjall volcanic system on the Reykjanes Peninsula (RP), producing a low-intensity effusive basaltic eruption (Pedersen et al., 2022). The eruption was preceded by month-long cycles of subsidence and uplift at the Svartsengi geothermal field, as well as the Reykjanes and Krýsuvík systems (see figure 2.1), which led to the eruption 8 km west in Fagradalsfjall (Flovenz et al., 2022; Sigmundsson et al., 2022).

Halldórsson et al., (2022) show, through thermobarometry of glass and clinopyroxene crystals, that the initial eruptive material was sourced from a depth of approximately 8 km, while after the 28th of April, the start of the fountaining phase of the eruption, the eruptive material was derived from a depth of about 15-20 km, near the Moho. Their study also indicates that the magma underwent rapid compositional changes in the early stages of the eruption, starting off with incompatible element depleted melt, which progressively got replaced with more incompatible element enriched melt.

The 2021 Fagradalsfjall eruption ended in September of 2021, after six months of activity. On the 3rd of August 2022, the second Fagradalsfjall eruption took place, lasting for eighteen days and ending on the 21st of August, and is believed to be an extension of the 2021 eruption (Marshall et al., 2023). In 2023, on the 10th of July, a third eruption took place near Litli-Hrútur, approximately 4 km NE of Fagradalsfjall. On 18th of December in 2023, a fourth eruption took place near Sundhnúkagígar, which lasted only a few days. Seismic activity and ground deformation at the time of writing suggests that another eruption in the area around Sundhnúkagígar can be expected in the next months. It is important to study the recent volcanic activity on the RP, where most of the Icelandic population resides, so that we can learn to live in these new conditions and the possible dangers that they pose to residents and infrastructure.

1.1 Samples

For this thesis six samples were prepared: one tephra sample, one naturally cooled lava sample and one quenched lava sample for each eruption.

The samples from 2021 were obtained on the 6th of May, during the fountaining phase of the eruption. The tephra (G20210506-7) sampled is fallout from the plume from the day of sampling. The naturally cooled lava (G20210506-1) sample came from slabby pahoehoe crust, sampled from a warm flow. The naturally cooled lava had been on the surface for four days prior to sampling. The quenched lava (G20210506-3) was sampled from a slow moving, viscous a'a flow, which had been on the surface for at least two days, but possibly up to seven days. The lava was sampled by Edward Marshall and the tephra was sampled by Alberto Caracciolo and Andrea Ricci.

The samples from the 2022 eruption were obtained on the 5th of August, two days after the start of the eruption. The tephra sample (G20220805-4) came from plume fallout, which was collected from the ground, some falling while still hot. The naturally cooled lava

(G20220805-6) was sampled from pahoehoe crust, which had been on the surface since the day before. The quenched lava (G20220805-3) was sampled from a single pahoehoe breakout, which likely erupted on the day of sampling, but possibly the day before. All samples from 2022 were collected by Alberto Caracciolo, Enikő Bali, Ella Wulfsberg Stokke, Sóley Johnson and Nicolas Levillayer.

1.2 The effect of microlite crystallization on melt composition and derived temperature

In basaltic systems, crystallization is controlled by composition, pressure, temperature, and time (Deardorff and Cashman, 2017). Microlites are small crystal phases with length of <100μm (Lofgren, 1974). Microlite crystallization usually occurs during magma ascent in the conduit due to large degrees of undercooling (Martel et al, 2006). Examinations of microlites within samples of eruptive materials are often used to interpret eruption dynamics (Haldeman, 2018, and references therein). Microlite crystallization processes are different between basaltic and silicic eruptions. In silica-rich melts, where the growth of crystals is generally slow, it is valid to assume that no crystal formation occurs during standard cooling or quenching (Szramek et al, 2010; Haldeman, 2018). However, in basaltic melts, microlites can nucleate and grow at cooling rates as fast as 1000°C/hour, relating to the diffusion rates being higher and viscosities lower in basaltic magmas compared to silica-rich ones (Haldeman, 2018; Lofgren, 1980; Cashman, 1993; Lesher et al., 1999; Szramek et al., 2010). This means that microlite formation is not limited to the magma ascent in the conduit and can occur in lava on the surface. Eruptive products from the Laki eruption in 1783-1784 show this quite clearly; tephra from the vents contain few microlites, since it has been ejected from the vents and cooled too quickly to allow microlite formation, while lava flow selvages from the same eruption are rich in microlites (Guilbaud et al., 2007).

Few studies have been done on the effect of microlite crystallization on groundmass glass compositions and how that affects the derived temperatures of the melt. However, some studies have shown that microlite/crystal growth cause distinct changes in the melt compositions (e.g. Guilbaud et al., 2007; Thordarson et al., 1996). It is therefore curious to see what effect microlite crystallization has on the derived temperatures of melt from different samples from the same eruption when using thermometers based on the composition of the melt/minerals. The purpose of this thesis is to test how microlite crystallization affects calculated magma temperatures in practically the same magma, but different types of samples which cooled differently on the surface from the 2021 and 2022 Fagradalsfjall eruptions.

2 Geologic setting and previous studies

Situated on the Mid-Atlantic Ridge (MAR), Iceland exists due to the proximity of a hotspot to the rift (Schilling, 1973), causing the MAR to splinter into rift- and transform zones between northeast and southwest Iceland (Jakobsson et al., 2008). Volcanic zones sit on- and off-rift, with the on-rift zones being characterized by geochemically depleted, tholeiitic lavas, and the off-rift zones being characterized by geochemically enriched, transitional to alkalic lavas (Jakobson et al 2008). The Reykjanes Peninsula (RP) is a structural continuation of the Reykjanes Ridge (RR), which becomes oblique to the spreading direction of the ridge as it approaches Iceland (see Figure 2.1). This is thought to be due to the proximity to the Iceland hotspot (Jakobsson et al., 2008).

2.1 The Reykjanes peninsula

The RP is a trans-tensional plate boundary including transform faulting and spreading, the only known on-land example of the sort (Sæmundsson et al., 2020). There are several volcanic systems from the centers of which northeast and southwest fissure swarms extend (Sæmundsson et al., 2020). Generally, five volcanic systems are considered to exist on the RP. These are, from west to east; Reykjanes, Eldvörp-Svartsengi, Fagradalsfjall, Krýsuvík and Brennisteinsfjöll, as seen in Figure 2.1 (Sæmundsson et al, 2020).

Only Krýsuvík displays features common to most central volcanoes and is the only volcanic system on the peninsula that has erupted large volumes of evolved tholeiite (Sæmundsson et al., 2020). The Brennisteinsfjöll system has been the most productive in the last 7000 years, considering the areal extent of lavas produced (Sæmundsson et al., 2020). The RP is mainly covered in basaltic lavas from postglacial periods of volcanism (Jakobsson et al., 1978; Gudmundsson, 1986), and these lavas are mostly olivine-tholeiites (Jakobsson et al., 2008).

In the past 4000 years, there have been three eruptive cycles on the RP, each lasting about 400-500 years, at time intervals of about 800-1000 years. The volcanic activity tends to affect one system at a time, jumping from east to west successively, with each jump spaced about 100-200 years apart (Sæmundsson et al., 2020). While there has not been any volcanic activity in the Fagradalsfjall system for 7000 years (Caracciolo et al., 2023; Sæmundsson et al., 2020), the RP has been quite active during the Holocene (Sæmundsson et al., 2020). The last eruption period, prior to the one that started in 2021, lasted from about 800 CE to 1240 CE and affected all volcanics systems on the RP, excluding the Fagradalsfjall system (Caracciolo et al., 2023; Sæmundsson et al., 2020; Sigurgeirsson, 2004, 1995).

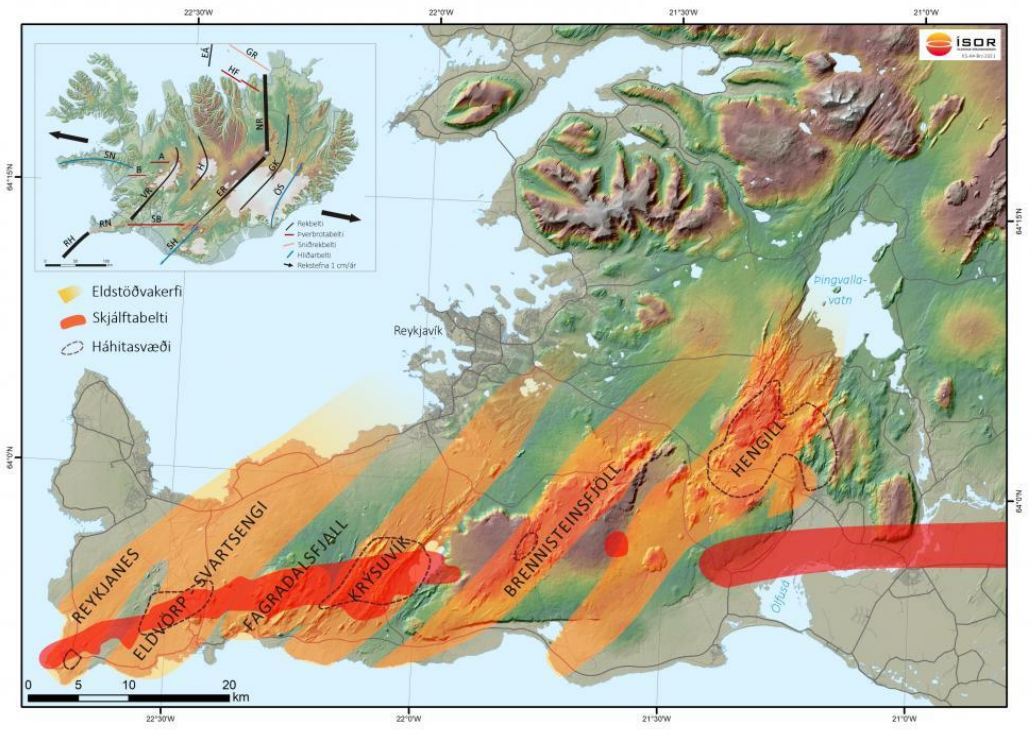

Figure 2.1.1: The volcanic systems of the Reykjanes peninsula. From Sæmundsson and Sigurgeirsson (2013).

3 Methods

3.1 Sample preparation

Lava, both naturally cooled and quenched, and tephra samples from May 6th, 2021, and August 5th, 2022, had already been collected. Epoxy mounts were created from each of the samples by choosing small grains from each sample and suspending them in epoxy within a 1-inch diameter mold. Once the epoxy had dried and hardened, the samples were taken out of the mold and cut in half. One half was selected, usually the one with the most exposed surface of sample, and that half polished using sandpaper with decreasing roughness, and finally with Kemet Diamond Compound KD-C2 of 3 and 1 microns. Once polished, they were coated with a thin layer of carbon, which acts as a conducting medium for the electron beam in the Scanning Electron Microscopy (SEM) and Electron Probe Micro-Analyzer (EPMA). The samples were kept in a dust free cabinet at a constant humidity while not being analyzed in the SEM or EPMA, to prevent impurities settling on the surface, or damage of the carbon coating.

3.2 Scanning Electron Microscopy (SEM)

The main purpose of using the SEM in this thesis was to take pictures of the samples, its groundmass, and phenocrysts, to be analyzed using the image processing software ImageJ. The SEM was also used to briefly pre-scan the samples before using the EPMA.

The SEM in question is a Hitachi Tabletop Microscope TM3000 SEM which has a Quantax energy dispersive spectrometer (EDS), located at the Institute of Earth Sciences at the University of Iceland. An acceleration of 15kV with a tungsten filament, 30 nm resolution and a magnification of 200x was used.

3.3 Electron Probe Micro-Analyzer (EPMA)

The main purpose of using the EPMA was to determine the chemical compositions of minerals and groundmass glass in the samples. The analysis was conducted at the Institute of Earth Sciences at the University of Iceland using a JEOL JXA-8230 Superprobe equipped with a LaB6 thermionic electron emitter, and five wavelength-dispersive spectrometers (WDS). The glass in the samples was analyzed using a beam with a diameter of 10 μm, while the mineral compositions were analyzed using spot analysis, in which the analytical conditions in all sessions were identical to those described in Halldórsson et al. (2022).

Multiple points were analyzed in four samples, one lava sample from each eruption and the tephra samples from each eruption. The glass was analyzed by choosing mineral free areas in the groundmass. Olivine (ol), clinopyroxene (cpx) and plagioclase (plag) minerals were

also analyzed; minerals representative of each size range, and zonations that occurred in the larger crystals.

Elemental maps of the groundmass were also collected in the EPMA, to assess the ratio of the minerals, since ol and cpx microlites in the groundmass were difficult to tell apart using only back scattered electron (BSE) images. Maps were collected showing the distribution of the elements Ca, Mg, Fe, Cr and Na, of which the calcium and magnesium maps were the most useful to determine the ratio of ol/cpx, since these elements occur in very different quantities in these minerals.

3.4 ImageJ

The main purpose of using the image editing software ImageJ was to analyze the Back scattered electron (BSE) images taken in the SEM to determine the crystallinity of the samples and the size distribution of the minerals.

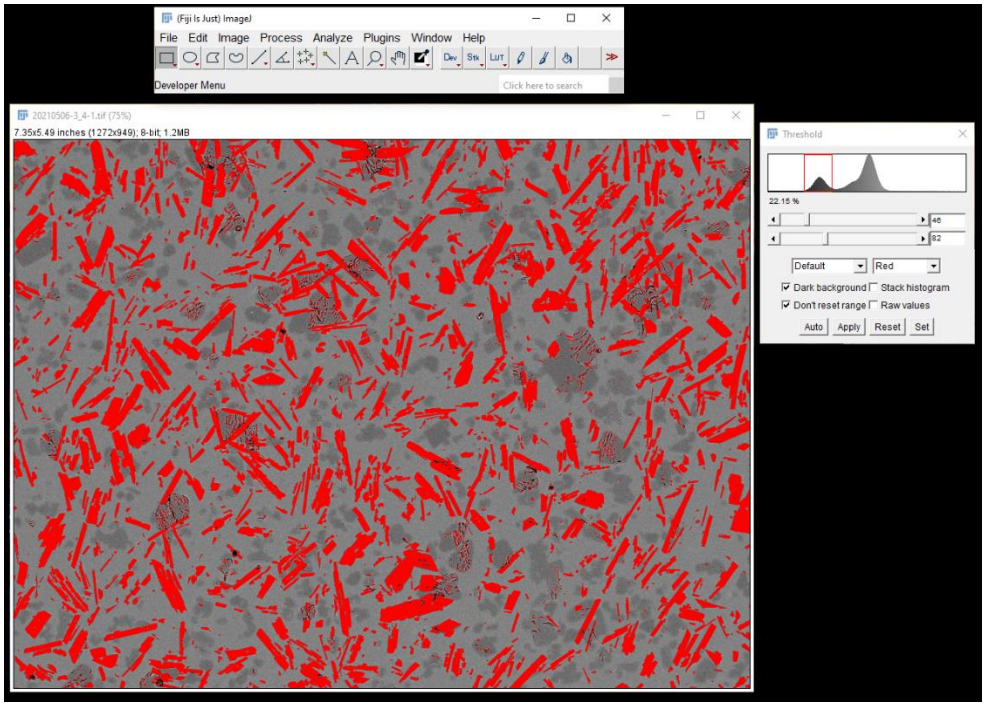

Figure 3.4.1: Volume proportion of plagioclase microlites within the groundmass of the 2021 lava determined using the "Threshold" command in ImageJ. Judging by this, the volume percentage of plagioclase is about 22%.

To determine the crystallinity of the samples, the "Threshold" command under "Image" < "Adjust" in ImageJ was used as demonstrated in Figure 3.4.1, where each phase was analyzed individually (vesicles and cracks, glass, ol and cpx together and plag) in multiple pictures for each sample, and the average ratio was calculated using Microsoft Excel. As mentioned in the chapter before, it was difficult to tell apart the ol and cpx from the BSE images, so to determine the ratio of ol/cpx elemental maps from the samples obtained in the EPMA were converted to grayscale in ImageJ, and then the "Threshold" command used

same as described above. Figure 3.4.2 shows an original elemental map of Mg and a converted and edited elemental map used to determine the mineral ratios.

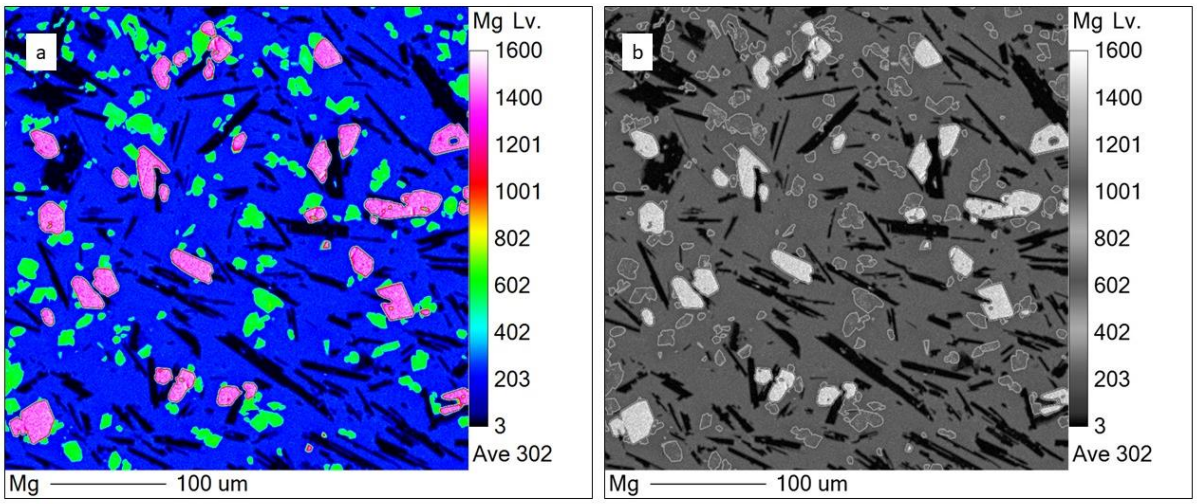

Figure 3.4.2: a) Elemental map showing Mg distribution in lava groundmass sample from 2021, where olivine is pink, clinopyroxene is green, plagioclase is black, and the glass is blue. b) A converted grayscale image of the same elemental map, where the olivine is now white, clinopyroxene a darker gray, plagioclase is black, and the glass is a lighter gray.

To determine the size distribution of the minerals the scale of the images had to be set. Under all the back scattered electron images was a scale representing 500 µm. Using the "Straight" command, to draw a line over the scale bar and setting the scale through "Analyze" < "Set Scale". From there the "Threshold" command was used again to highlight each individual phase and clicked on "Apply" to get a black and white image, where the white represented the relevant minerals (plag and dark minerals) and black representing everything else. From there I used "Process" < "Filters" < "Median" and set the radius to 2-3 pixels to filter out all the dots that weren't part of the mineral assemblage. If necessary, I used the "Paintbrush Tool" to paint in black over the remaining dots that weren't showing the relevant minerals or used white to fill in the minerals where necessary.

3.5 Thermobarometry

3.5.1 Thermometry

There exist many types of thermometers that are used to estimate the temperature of magma. These thermometers use the chemical compositions of the melt and/or the minerals in various ways to make the estimations (see Putirka, 2008). Putirka (2008) assessed all existing thermometers at the time. Here I selected two of the thermometers described by Putirka (2008), equations (13) and (16). Equation (13) because of its simplicity and independence of pressure and equation (16) because of its higher accuracy for samples with compositions like ones prepared for this thesis.

In 1987, Helz and and Thornber put forth a simple thermometer which depends only on the wt% of MgO in a liquid:

$$T(°C) = 26.3\mathrm{MgO}^{liq} + 994.4\ °C \qquad (13) \qquad \text{(eqn1)}$$

This thermometer has an uncertainty of ± 71°C and requires olivine as an equilibrium mineral phase with the liquid. It is possible to lower this uncertainty by taking more compositional terms into account (Putirka, 2008). An improvement was suggested by Yang et al. (1996), by requiring that additional phases be in equilibrium with the liquid:

$$T(°C) = -583 + 3141\left[X^{liq}_{SiO_2}\right] + 15779\left[X^{liq}_{Al_2O_3}\right] + 1338.6\left[X^{liq}_{MgO}\right] - 31440[X^{liq}_{SiO_2} \cdot X^{liq}_{Al_2O_3}] + 77.67\left[P(\mathrm{GPa})\right] \qquad (16) \qquad \text{(eqn2)}$$

where terms like X_{MgO}^{liq} represent the mole fraction of MgO in the liquid. Equation (16) performs best for liquids in equilibrium with ol + plag + cpx, but less well for liquids saturated with other phases such as oxides like spinel. The uncertainty for equation (16) is ± 26°C.

The pressure values used for the P-dependent equations were calculated using Olivine-Plagioclase-Augite-Melt (OPAM-) barometry as described in the chapter below.

3.5.2 Olive-Plagioclase-Augite-Melt (OPAM-) barometry

The magma storage depths were estimated using the olivine-plagioclase-augite-melt (OPAM) barometer (Yang et al., 1996), using the pyOPAM code by Baxter et al (2023) which is the further development of the OPAM implementation of Hartley et al. (2018). This barometer allows estimations of the pressure at which a melt was last in equilibrium with the crystal cargo, given that the melt is saturated with ol, plag and cpx (Yang et al., 1996). Using the pyOPAM code, melt compositions that are not saturated by three phases can be filtered out (Baxter et al., 2023; Hartley et al., 2018). The first step of the code is the calculation of χ^2 misfit between cation fractions of X_{Mg}, X_{Ca}, and X_{Al} and those predicted by the OPAM equations in Yang et al. (1996). The probability of fit (Pf), is assessed using the minimum χ^2. If the composition of the melt deviates from three-phase saturation, the Pf value is low. Melt compositions returning Pf values higher than 0.8 are likely to fall on or are near the OPAM boundary and can be used for estimating pressure (Hartley et al., 2018).

By arranging the compositional data of the samples into Microsoft Excel, one could run that data through the pyOPAM code, and it returns values for pressure and Pf. Taking the average pressure of the values with a Pf value larger than 0.8, one could use those pressure estimates to calculate the magma temperature, as described in the chapter above.

3.6 Recalculated melt

As mentioned in Chapter 1.2, microlite crystallization can greatly affect the melt composition. For these reasons, it is interesting to see what the melt composition may have

been before the crystallization of microlites. One way to do this is to recalculate the melt composition by adding back the compositions of the microlites into the melt. To do this, one must have a few values at hand: The volume proportions of each microlite mineral and glass, the average compositions of the microlites and glass, and the densities of each mineral and the glass. The recalculated melt composition is calculated by multiplying the volume percentage (Vol%) of minerals and glass with their densities, dividing the number for each phase with the sum of all the phases to get the weight percentage (Wt%) of each phase in the lava, and finally multiplying each phase weight total percentage with the amount of each element in each phase before adding them all together. This process is demonstrated below in Tables 3.6.1 and 3.6.2, using the results for the 2022 lava. The mineral densities used for these calculations were obtained from the database of mindat.org, while the basalt densities were calculated using Petrolog (Danyushevsky & Plechov, 2011) from petrologsoftware.com according to Lange and Carmichael (1987), using the average tephra and lava glass compositions from both eruptions.

	Ol ($Fo_{75}Fa_{25}$)	**Cpx (augite)**	**Plag (bytownite)**	**Glass (basalt)**	**sum**
Vol %	1.4	7.1	13.3	78.2	100
Densities	3.55	3.20	2.74	2.71	-
Wt%	4.97	22.72	36.44	211.92	276.05
Wt% norm	0.02	0.08	0.13	0.77	1

Table 3.6.1: Weight total percentage (Wt%) for each phase in the 2022 lava calculated. The densities of each phase, in this case olivine (Fo75Fa25), clinopyroxene (augite), plagioclase (bytownite) and glass (basalt), are multiplied with the volume percentage to find the Wt%. The Wt% is then normalized.

	SiO_2	**TiO_2**	**Al_2O_3**	**FeO_t**	**MnO**	**MgO**	**CaO**	**Na_2O**	**K_2O**	**Cr_2O_3**
Ol	39.20	0.03	0.05	17.80	0.27	42.26	0.47	0.00	0.00	0.04
Cpx	52.28	0.82	4.39	7.27	0.17	16.27	19.13	0.24	0.00	0.44
Plag	50.32	0.07	31.53	0.86	0.01	0.32	14.57	2.86	0.11	0.00
Glass	49.67	1.63	14.08	11.70	0.20	7.19	12.67	2.15	0.46	0.00
Recalculated melt	***49.78***	***1.33***	***15.33***	***10.01***	***0.17***	***7.66***	***13.23***	***2.05***	***0.37***	***0.04***

Table 3.6.2 The recalculated melt compositions are derived using the compositions of each phase. If we take SiO_2 for example, its amount in the recalculated melt would be $Ol_{Wt\%}$ * Ol_{SiO2} + $Cpx_{Wt\%}$ * Cpx_{SiO2} + $Plag_{Wt\%}$ * $Plag_{SiO2}$ + $Glass_{Wt\%}$ * $Glass_{SiO2}$.

3.7 Equilibrium compositions of minerals within melt

The equilibrium compositions of the minerals (ol, cpx and plag) with the tephra and lava glass compositions, as well as the recalculated melt compositions, were calculated and compared to the average microlite and micophenocryst rim and core compositions of the minerals analyzed in the samples. For ol we consider the Fo-content, for cpx the Mg# and for plag the An-content. The Fe/Mg ratio of an equilibrium crystal can be calculated if both the Fe-Mg exchange coefficient (Kd) and the melt Mg# or Fe/Mg is known (e.g.: Bédard, 2010). The Kd value is calculated using the following equation:

$$Kd^{Mineral/Melt} = (XFe/XMg)^{Mineral} / (XFe/XMg)^{Melt} \quad \text{(eqn3)}$$

In this study, the Kd value of 0.3 ± 0.03 was used for calculating the equilibrium composition of ol, while the Kd value of 0.27 ± 0.03 was used for cpx (Roeder and Emslie, 1970; Bédard, 2010). The equilibrium compositions for ol and cpx were calculated using the following equation:

$$(Mg/Fe^{Mineral} / (Mg/Fe^{Mineral} + 1)) * 100 \quad \text{(eqn4)}$$

with the Mg/Fe Mineral being calculated using the following equation:

$$Mg/Fe^{Mineral} = \frac{(\frac{MgO}{40.3})/((\frac{Fe^{2+}}{Fe^{3+}})*(\frac{FeO}{71.84}))}{Kd} \quad \text{(eqn5)}$$

Fe^{2+}/Fe^{3+} ratio in the melt was set to 0.9.

For plag, the equilibrium An-content was calculated using Equation 33 from Namur et al (2012):

$$X_{An} = -2.71 + \left[0.55Si_8 - 0.04Al_8 + 0.35Fe_8 + 0.19Mg_8 + 0.19Ca_8 + 0.45Na_8\right] + \left[1.09\frac{Ca_8}{Ca_8 + Na_8} + 3.68\frac{Al_8}{Al_8 + Si_8}\right] \quad (33) \quad \text{(eqn6)}$$

Equation 33 from Namur et al (2012) is calibrated for plagioclase liquid pairs in mafic-ultramafic melts.

4 Results

4.1 Petrography

Plagioclase (plag), olivine (ol) and clinopyroxene (cpx) are all present in the samples from 2021. The plag, which is the most abundant mineral, is generally euhedral and elongated (Fig. 4.1.2 and 4.1.3). The plag microlite size in the tephra and lava groundmass ranges from 3 – 100 μm, while the microphenocrysts (mpc‘s) were up to 270μm in length. The ol and cpx were also mostly euhedral, in contrast with the plag their shapes are more isometric with a size range around 5 – 40 μm, in diameter (Fig. 4.1.2). The size of ol mpc‘s ranged from 70 – 300 μm, and there were no mpc‘s of cpx present. A few Cr-spinel mpc‘s where also present in both the tephra and lava. Glomerocrysts of plag, cpx and ol microlites were common in the groundmass.

In the 2022 samples, plagioclase, olivine and clinopyroxene are all present like in the samples from 2021. Plag is the most common mineral, both as microlites in the groundmass and as mpc’s. The crystals are generally euhedral and elongated. The microlites in the tephra and lava groundmass range from 3 – 100 μm same as in the 2021 samples, while the mpc’s reached sizes up to 500 μm. The ol and cpx were mostly isometric and subhedral, the microlite size ranged from 5 – 70 μm, while the mpc’s of ol reached sizes from 100 – 500 μm. Glomerocrysts were common, both in the groundmass and in mpc’s.

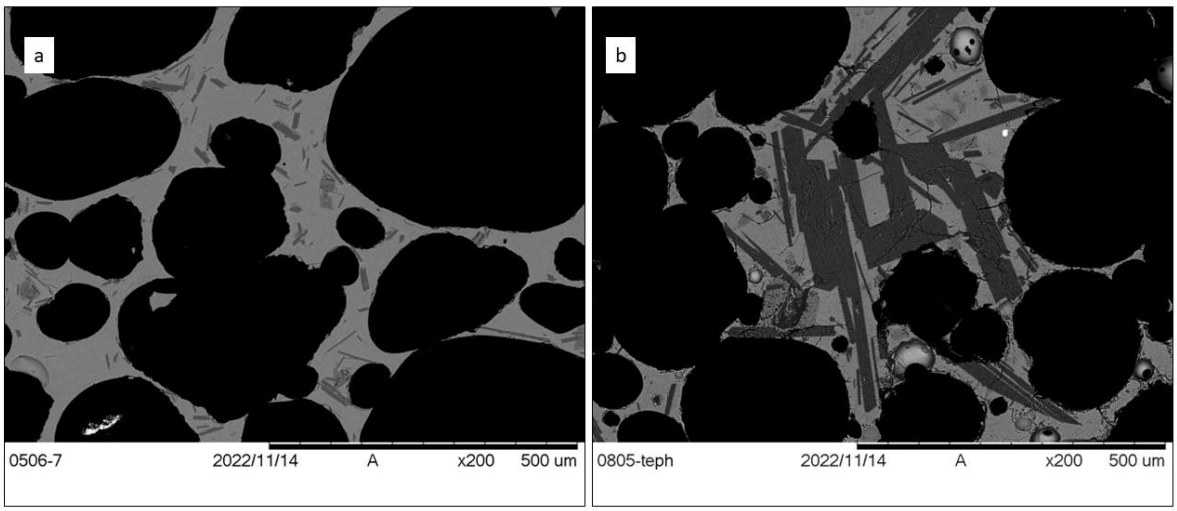

Figure 4.1.1: a) BSE image of 2021 tephra sample and b) BSE image of 2022 tephra sample. Black represents vesicles, the groundmass glass is light gray, the darker gray elongated minerals within the groundmass are plag, and the lighter gray minerals, sometimes hard to distinguish from the groundmass, are both ol and cpx. Bright mineral in b) is Cr-spinel.

Back scattered electron (BSE) images of the 2021 samples (see Figure 4.1.1) reveal a highly vesicular tephra with a non-crystalline groundmass but containing the occasional (mpc) of ol, plag and Cr-spinel. Analysis of the back scattered electron images suggests a vesicularity of around 82%. The tephra groundmass is 90% glass and 10% microlites: 6.1% plagioclase (plag), 1.9% olivine (ol) and 2.0% clinopyroxene (cpx).

BSE images of the 2022 samples (see Figure 4.1.1) reveal a highly vesicular tephra with a crystalline groundmass, also containing many mpc of plag, and occasionally ol, cpx and Cr-spinel. Analysis of the back scattered electron images suggests a vesicularity around 81%, slightly lower compared to the tephra from 2021. The tephra groundmass is 84% glass and 16% minerals: 9.8% plag, 1.0% ol and 5.2% cpx.

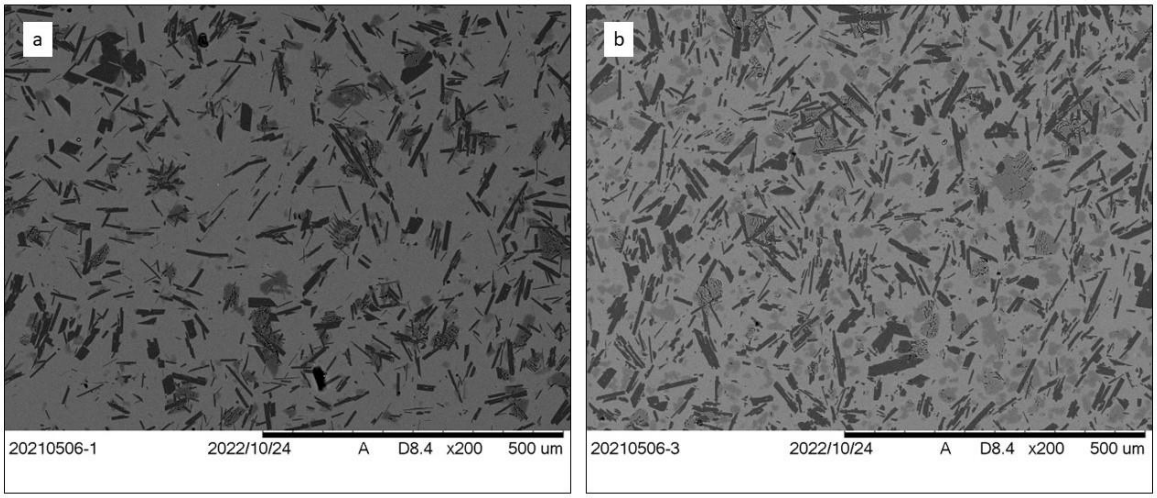

Figure 4.1.2: BSE images of lava samples from the 2021 eruption. a) The quenched lava, b) the naturally cooled lava. The glass is light gray, the darker gray elongated minerals within the groundmass are plag, and the lighter gray minerals, sometimes hard to distinguish from the groundmass, are both ol and cpx. These images show that the naturally cooled lava has significantly more microlites within the groundmass compared to the quenched lava.

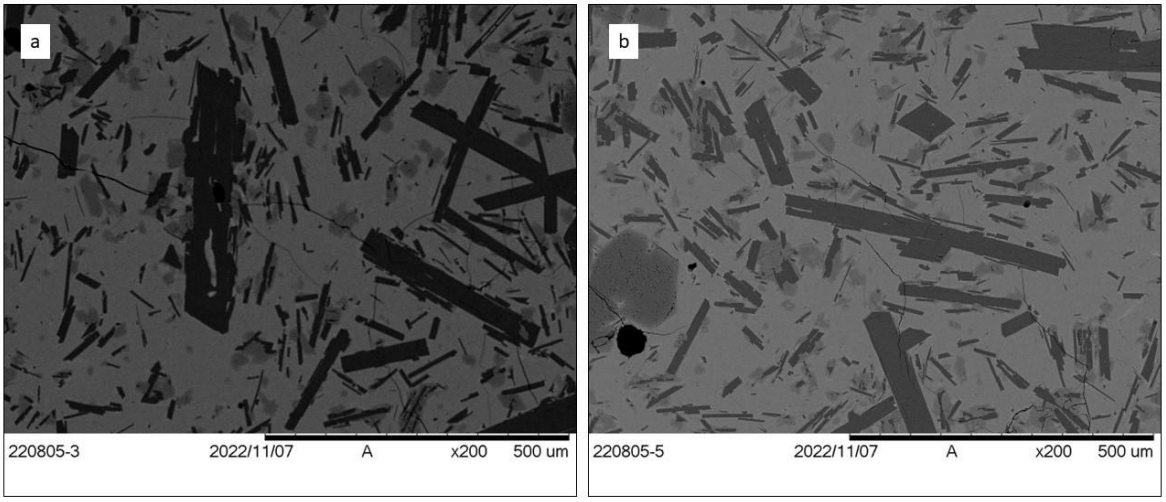

Figure 4.1.3: BSE images of lava samples from the 2022 eruption. a) The quenched lava, b) the naturally cooled lava. The glass is light gray, the darker gray elongated minerals within the groundmass are plag, and the lighter gray minerals, sometimes hard to distinguish from the groundmass, are both ol and cpx. These images show little differences between the two lava samples.

There is some observable difference between the naturally cooled lava and the quenched lava in the samples from 2021, as seen in Figure 4.1.2. The lava samples are revealed to be non-vesicular and relatively crystalline compared to the tephra. The groundmass in the naturally cooled lava is 64% glass and 36% minerals: 22% plag, 6.8% ol and 7.3% cpx microlites. The groundmass in the quenched lava is 78% glass and 22% minerals: 13.4%

plag, 4.1% ol and 4.5% cpx. Some mpc of ol, plag and Cr-spinel are present. Figure 4.1.4 shows the average groundmass crystallinity of the naturally cooled lava and the tephra from 2021.

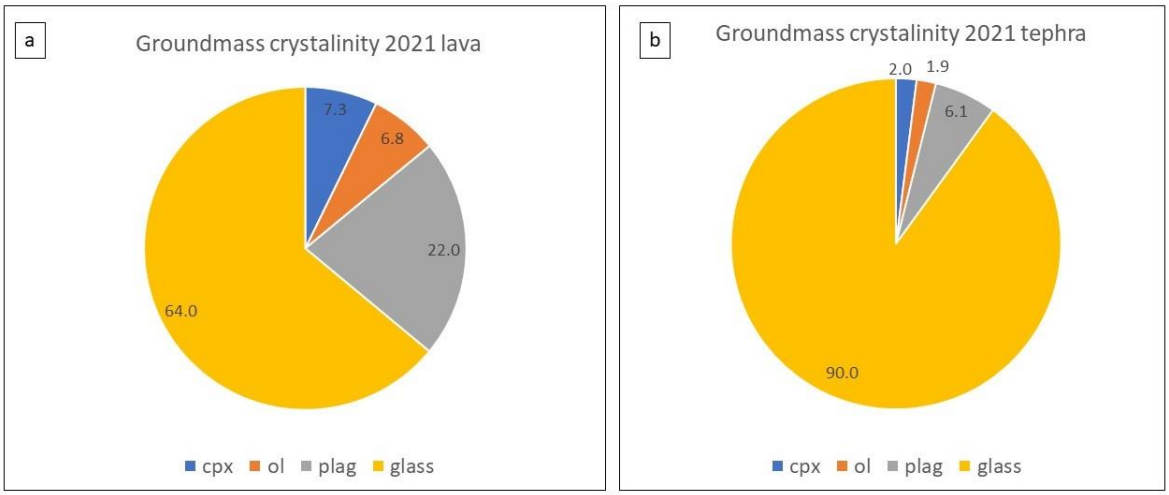

Figure 4.1.4: The average groundmass crystallinity of the 2021 naturally cooled lava and tephra.

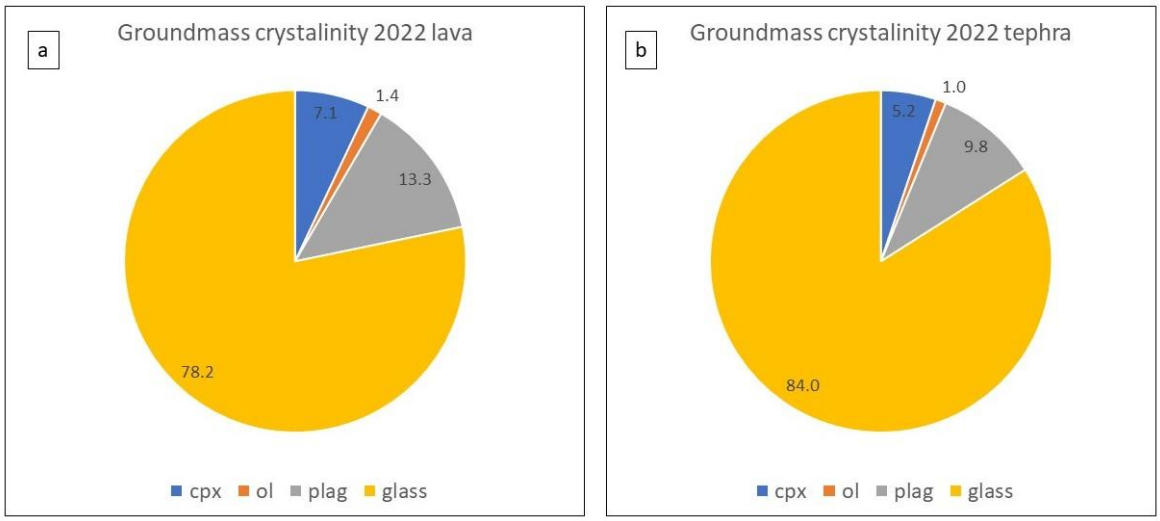

Figure 4.1.5: The average groundmass crystallinity of the 2022 naturally cooled lava and tephra. Note, these do not include the common microphenocrysts.

In contrast, there is little to no observable difference between the lava samples in the samples from 2022. Both the naturally cooled lava and the quenched lava are revealed to be non-vesicular and crystalline, as seen in Figure 4.1.3. The groundmass, not including the mpc's, is 78.2% glass and 21.8% minerals: 13.3% plag, 1.4% ol and 7.1% cpx microlites. Including the mpc, which are mostly plag, the ratio is 62% glass and 38% minerals, with the ratio of mpc's being about 65% plag, 35% ol and <1% cpx. Mpc's of ol, plag and Cr-spinel are present, with large mpc's of plag being very common. Figure 4.1.5 shows the groundmass crystallinity of the 2022 naturally cooled lava and tephra.

When compared, it becomes apparent that the 2022 samples, both the tephra and the lava, contain much larger amount of microlites and microphenocrysts (mpc's) than the samples from 2021. However, there is a much bigger difference between the crystallinity of the 2021 and 2022 samples. The 2021 tephra is barely crystalline while the 2021 lava contains abundant microlites. In contrast, the crystallinities of the 2022 tephra and lava are very similar. The 2022 samples contain a much larger ratio of cpx to ol, where it is around 5cpx/1ol, compared to the 2021 samples, where the ratio is about 1cpx/1ol. The ratio of plag to ol+cpx is somewhat similar in samples from both 2021 and 2022.

4.2 Chemical composition

The chemical compositions of the glass, plag, ol and cpx were obtained by EPMA. Figure 4.2.1 shows a Fenner-type diagram of the TiO_2 against MgO contents of the glass in the different samples.

The glass in the 2021 tephra sample contained an average of 8.37% MgO, 1.22% TiO_2 and 0.33% K_2O, while the glass in the lava samples had an average of 6.79% MgO, 1.65% TiO_2 and 0.41% K_2O (see Appendix A for full chemical content of all samples). The glass in the tephra from 2021 has the most primitive composition, while the glass in the lava from 2021 is the most evolved. The glass compositions from the 2022 samples fall in between the 2021 lava and tephra glasses.

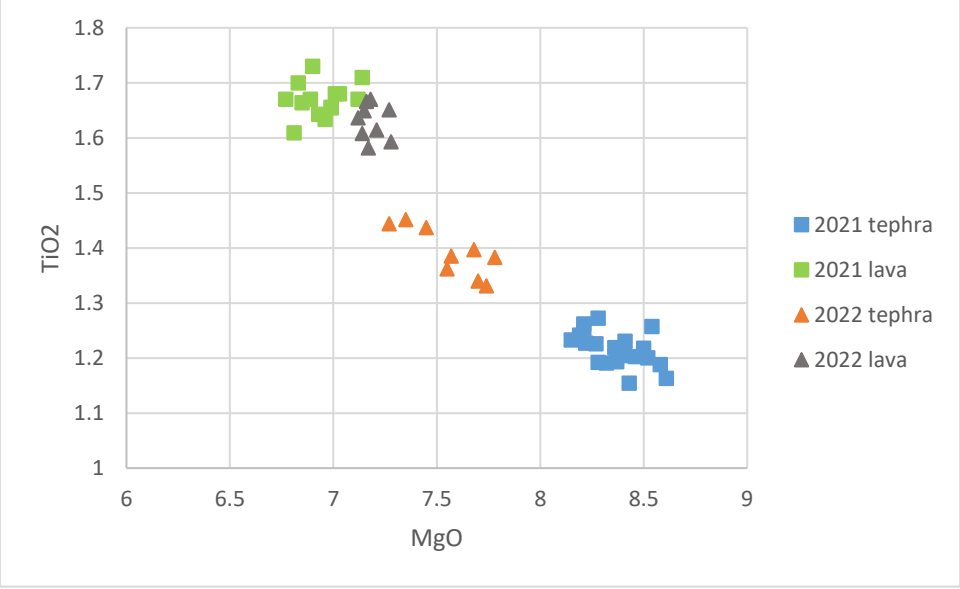

Figure 4.2.1: Fenner-type diagram of TiO_2 against MgO content of silicate glass analyzed in tephra and lava samples from 2021 and 2022.

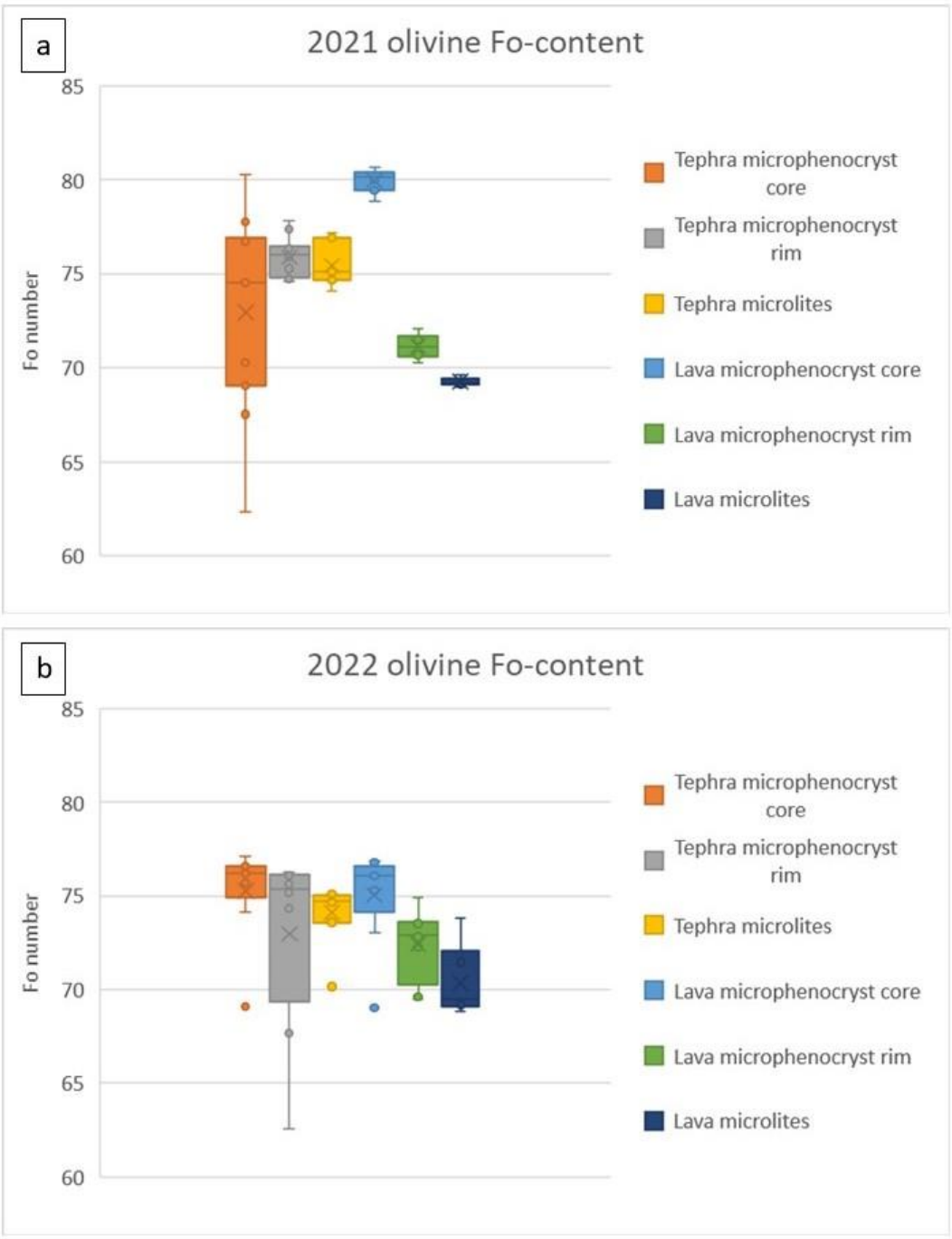

Figure 4.2.2: Comparison of Forsterite-content in olivine minerals in the 2021 (a) and 2022 (b) tephra and lava samples. The Fo-content is calculated by using the Mg and Fe cation proportions of the minerals, through Mg/(Fe+Mg) *100. The box represents the interquartile range of the data set (Q1 to Q3). The line inside shows the median value. The whiskers that extend from the box show the range of data, excluding the outliers. The dots represent the outliers, which are data points that fall outside the expected range.

Figure 4.2.2 shows diagrams of the Fo-content of the olivines in the 2021 and 2022 samples, the tephra and lava mpc cores, rims and microlites. The Fo-content is calculated using Mg and Fe cation proportions, obtained in the EPMA, through Mg/(Fe+Mg)*100. The tephra from 2021 has ol with content of $Fo_{62-80}Fa_{20-38}$, and lava with $Fo_{69-81}Fa_{19-31}$ (Fig.4.2.2.a). There is considerable difference between Fo-content variations between the lavas and the

tephra. In 2021, the tephra mpc cores, rims and microlite compositions all overlap, with the cores having less primitive compositions in some cases than the rims and microlites. However, in the lava from 2021, the cores, rims and microlites do not overlap at all. The ol mpc cores in the lava are more primitive than all analysed minerals in the tephra, and vastly more primitive than the rims and microlites in the lava. The lava mpc rims and microlites overlap with the least evolved compositions in the tephra mpc cores.

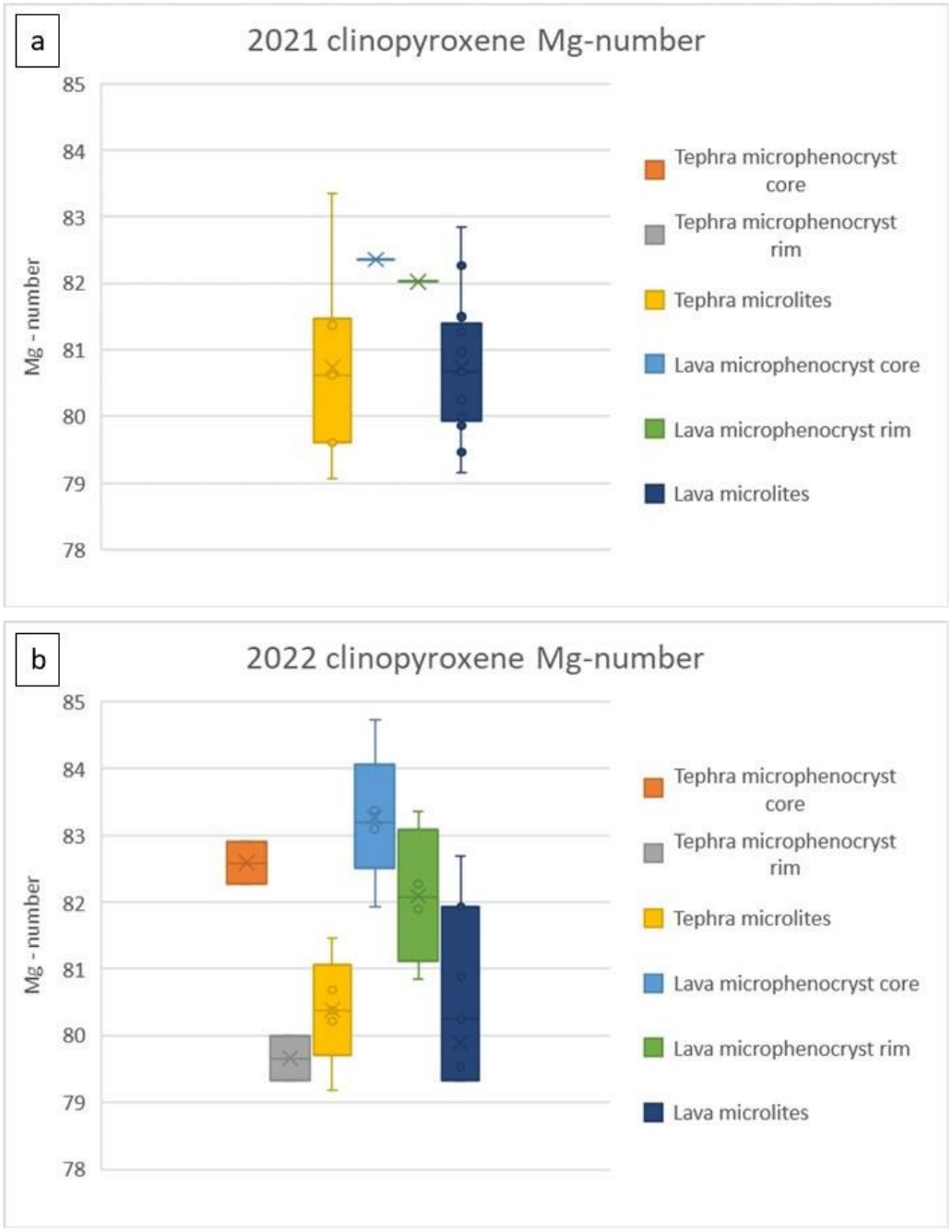

Figure 4.2.3: Mg-number of clinopyroxenes in the 2021 (above) and 2022 (below) samples. Mg-number is calculated using the Mg and Fe cation proportions of the mineral, through Mg/(Fe+Mg) *100. See description under Figure 4.2.1 for explanation of the box and whiskers diagram.

In contrast, the Fo-content in the ol from the 2022 samples has much less variety than the samples from 2021 (Fig. 4.2.2.b). The tephra from 2022 has an ol content of $Fo_{63-77}Fa_{23-37}$ and in the lava $Fo_{69-77}Fa_{23-31}$. Like in the tephra from 2021, the 2022 tephra mpc cores, rims and microlites all overlap, with the cores being only slightly more primitive than the microlities, and the rims having the most variable and evolved compositions. The lava mpc rims and microlites overlap, with the mpc rims being slightly more primitive than the microlites. The cores in the lava are the least evolved, but overlap with the mpc cores analysed in the tephra.

When compared, it becomes apparent that in both 2021 and 2022, the tephra ol mpc cores, rims and microlites overlap with each other, while in the lava the mpc cores are more primitive than the mps rims and microlites. However, there is much less variability in the ol compositions in the 2022 samples.

Figure 4.2.3 shows diagrams of the clinopyroxene Mg-number in the 2021 and 2022 samples, the tephra and lava mpc cores, rims and microlites. The Mg-number is calculated based on the Mg and Fe cation proportions obtained in the EPMA, through Mg/(Fe+Mg)*100.

The cpx in the 2021 samples classify as augite, with compositions of $Wo_{37-41}En_{48-50}Fe_{10-13}$ in the tephra and $Wo_{38-43}En_{46-51}Fe_{10-13}$ in the lava. Due to the small amount of mpc cpx's in the samples, it is more difficult to see a trend in the cpx compositions like the ones we see in the ol compositions. In the 2021 samples, no mpc's were observed in the tephra, and only a single mpc was observed in the lava. In this one mpc in the 2021 lava, the core is more primitive than the rim, and both are more primitive than the microlites found both in the tephra and in the lava. The microlites, both in the tephra and lava sample, have a near identical Mg-number and overlap completely.

The cpx in the samples from 2022 is also classified as augite. The cpx's in the tephra have compositions of $Wo_{31-44}En_{45-55}Fe_{11-14}$ and in the lava $Wo_{37-44}En_{45-53}Fe_{9-15}$. In the samples from 2022 some mpcs' were analysed both in the tephra and in the lava, along with multiple microlites. The mpc cores in the tephra are vastly more primitive than the mpc rims. The tephra microlites overlap with the mpc rims, but many microlites analysed had a more primitive composition than the mpc rims. In the lava from 2022, the mpc cores have the most primitive compositions. The mpc rims in the lava overlap slightly with the cores of both the lava and the tephra cpx mpcs'. The microlites in the lava have more variable compositions than the ones in the tephra, overlapping with the mpc rims in the lava and tephra, and with the microlites in the tephra. In the lava sample from 2022 overall from core to rim to microlite composition there seem to be a continuous compositional change towards more evolved compositions.

When compared, it becomes apparent that the cpx's from 2022 are somewhat more primitive than the ones from 2021 and have a more variable composition as well, though this might be caused by the significantly higher number of analyses from 2022.

Figure 4.2.4 shows a diagram of the An-content of the plagioclase in the samples from 2021 and 2022, the tephra and lava mpc cores, rims and microlites. The plag in the samples from 2021 are classified as bytownite. The plag in the tephra from 2021 has compositions of $An_{73-80}Ab_{4-26}Or_{0-1}$, and the lava $An_{72-76}Ab_{23-27}Or_{0-1}$. In the plag analysed from the 2021 samples, there is not much variability in compositions. The tephra mpc cores, rims and microlites all

overlap, with the rims having the most variability and being the most primitive. There were no mpc‘s analysed in the 2021 lava. The microlites in the 2021 lava overlap with all plag analysed in the tephra.

The plag in the 2022 samples are classified as bytownite. The plag in the tephra has compositions of $An_{74-82}Ab_{18-25}Or_{0-1}$, and the lava $An_{70-87}Ab_{13-30}Or_{0-1}$. There is much more variability in the plag analysed in the 2022 samples than in the 2021 samples. The plag in the tephra sample, mpc cores, rims and microlites, all overlap with eachother and have an almost identical composition. However, the plag in the lava has a much wider variability in composition. The mpc cores are the most primitive of all with a large variability in composition, with the most evolved cores overlapping with all the plag analysed in the tephra. The mpc rims in the lava overlap with the more evolved half of the mpc cores. The lava microlites are the most evolved of all, without overlapping with any other analysed plag in both tephra and lava.

When compared, the plag in the tephra from both 2021 and 2022 have similar compositions and little variability. It is difficult to compare mps’s in the 2021 and 2022 lava samples, since no mpc’s were analysed in the 2021 lava samples. The microlites in the 2021 lava are slightly more primitive than the ones in the 2022 lava.

Looking at the compositions of the minerals analysed in the tephra both from 2021 and 2022, they generally show an overlap regardless of textural position, with the cpx from 2022 being the only exception to this. In contrast, the mineral compositions in the lavas from 2021 and 2022, the mpc cores are generally the most primitive, the mpc rims are more evolved and the microlites have the most evolved compositions.

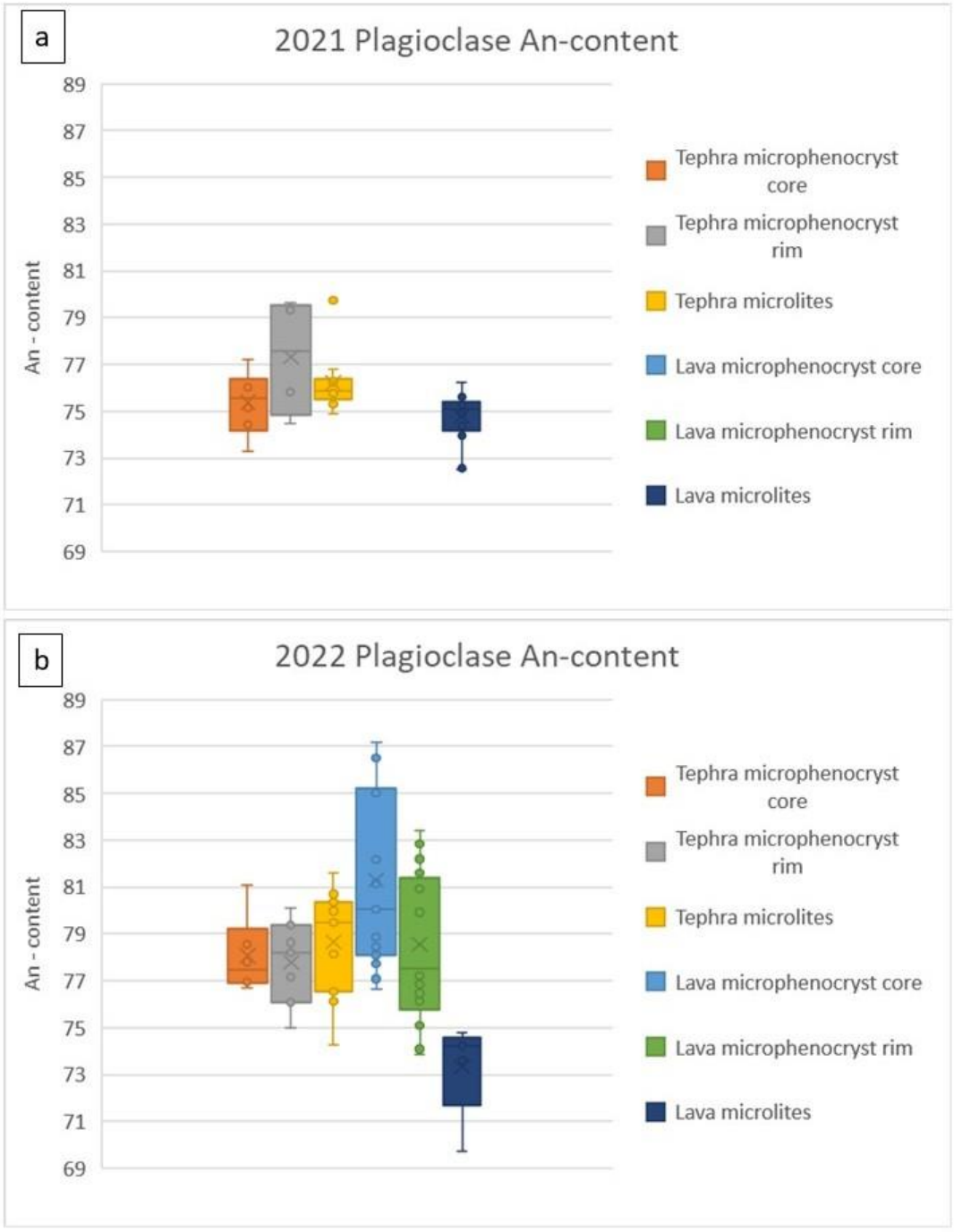

Figure 4.2.4: Anorthite-content of plagioclase in 2021 (above) and 2022 (below) samples. An-content is calculated using the Ca, Na and K cation proportions of the minerals, through Ca/(Ca+Na+K) *100. See description under Figure 4.2.1 for explanation of the box and whiskers diagram.

.

5 Discussion

5.1 Recalculated magma composition before microlite crystallization

Figure 5.1.1 shows a Fenner-type diagram of the TiO_2 against MgO content of the glass in the 2021 and 2022 samples, along with recalculated melt and whole rock compositions. The trend shown in this diagram suggests that fractional crystallization is responsible for this variability, with the melt composition becoming increasingly more evolved, as the minerals crystallize from it. The glass in the lava from 2021 is significantly more evolved than the glass from the tephra from the same year, and more evolved than the recalculated melt. The recalculated melt composition is more primitive than the glass analyzed in the fast cooled tephra. There is much less difference between the glass and melt compositions from 2022, correlating with the small amount of microlites crystallized in the lava over the tephra. The composition of the 2022 recalculated melt overlaps with the composition of the most primitive tephra glass compositions from 2022, but it is more evolved than the tephra from 2021. The whole rock compositions from 2022 (Caracciolo et al. unpublished) overlap with the more primitive 2021 tephra glass compositions. The 2021 recalculated melt plots close to the 2021 whole rock composition (from Halldórsson et al. 2021), which is more primitive than the 2021 recalculated melt composition. Neither of these overlap with other analyzed or calculated compositions.

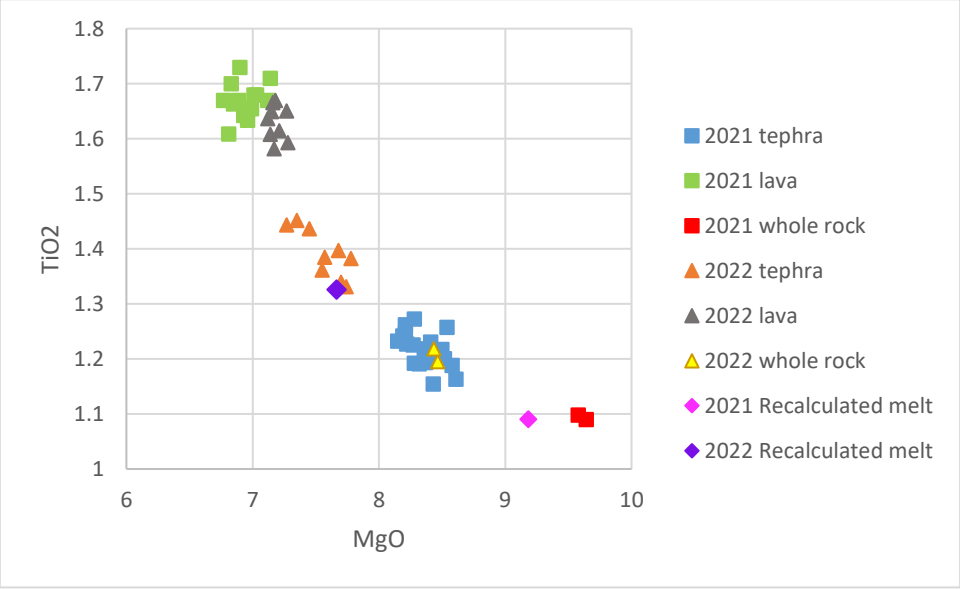

Figure 5.1.1: Fenner-type diagram of TiO2 against MgO in glass compositions from 2021 and 2022 tephra and lava samples, along with the compositions for the recalculated melt and the whole rock compositions of the samples.

Table 5.1.1 and 5.1.2 show the recalculated melt compositions for 2021 and 2022 respectively. It is apparent that the recalculated melt compositions from 2021 are more

primitive than the ones from 2022, with the MgO content from 2021 being 9.17, much higher than in 2022 which is 7.66.

2021	**SiO_2**	**TiO_2**	**Al_2O_3**	**FeO_t**	**MnO**	**MgO**	**CaO**	**Na_2O**	**K_2O**	**Cr_2O_3**
Ol	38.91	0.03	0.08	18.43	0.32	41.38	0.44	0.00	0.00	0.03
Cpx	51.34	0.66	3.63	7.01	0.18	16.47	19.88	0.20	0.00	0.60
Plag	49.41	0.07	31.71	1.01	0.01	0.31	14.87	2.71	0.09	0.00
Glass	49.95	1.65	13.12	12.22	0.22	6.79	11.79	2.03	0.41	0.00
Recalculated melt	***49.00***	***1.09***	***15.21***	***9.92***	***0.18***	***9.17***	***12.14***	***1.85***	***0.27***	***0.05***

Table 5.1.1: Recalculated melt compositions for the 2021 lava sample, calculated from the average microlite compositions of plag, ol and cpx + glass.

2022	**SiO_2**	**TiO_2**	**Al_2O_3**	**FeO_t**	**MnO**	**MgO**	**CaO**	**Na_2O**	**K_2O**	**Cr_2O_3**
Ol	39.20	0.03	0.05	17.80	0.27	42.26	0.47	0.00	0.00	0.04
Cpx	52.28	0.82	4.39	7.27	0.17	16.27	19.13	0.24	0.00	0.44
Plag	50.32	0.07	31.53	0.86	0.01	0.32	14.57	2.86	0.11	0.00
Glass	49.67	1.63	14.08	11.70	0.20	7.19	12.67	2.15	0.46	0.00
Recalculated melt	***49.78***	***1.33***	***15.33***	***10.01***	***0.17***	***7.66***	***13.23***	***2.05***	***0.37***	***0.04***

Table 5.1.2: Recalculated melt compositions for the 2022 lava sample, calculated from the average microlite compositions of plag, ol and cpx + glass.

5.2 Pressure and temperature calculations

Temperature estimates for the magma were calculated for the two eruptions using the chemical compositions of tephra and lava glass (only the naturally cooled lava for both eruptions) and for the recalculated melt, as is explained in Chapter 3.5.1. The results can be seen in Table 5.2.2 for 2021 and Table 5.2.3 for 2022. Table 5.2.1 shows the calculated pressures obtained through OPAM-barometry, which were used for the pressure dependent thermometer. As can be seen in Table 5.2.1, the probability fit for the pressure calculations varies between compositions. The compositions of glasses from tephra and lava samples from both years yield a high probability above 0.80. However, the probability fit for the recalculated melt from 2021 has a value of 0.64, and 0.28 for the 2022 eruption. According to Baxter et al. (2023), if the probability fit is above 0.80 the uncertainty of the pressure calculations is ±1.13 kbar, while if the probability fit is lower than 0.70 the uncertainty is

±2.07 kbar. Therefore, the calculated pressures for the recalculated melts have a higher uncertainty than the pressures calculated for the lava and tephra glass, meaning that the calculated temperatures for the recalculated melt based on the pressure dependent equations are not as reliable as the calculated temperatures for the lava and tephra glass.

	2021 tephra	**2021 lava**	**2021 recalc. melt**	**2022 tephra**	**2022 lava**	**2022 recalc. melt**
P in kbar	4.18	1.00	7.29	2.13	0.90	1.91
Probability	*0.94*	*0.94*	*0.64*	*0.81*	*0.92*	*0.28*

Table 5.2.1: Calculated pressures for 2021 and 2022 lava and tephra samples, as well as the recalculated melt compositions.

2021	**Lava glass**	**Tephra glass**	**Recalculated melt**	***Uncertainty***
Eq. 13	1173°C	1214°C	1236°C	*+/- 72°C*
Eq. 16	1160°C	1202°C	1243°C	*+/- 26°C*

Table 5.2.2: Calculated temperatures for the 2021 tephra, lava, and recalculated melt.

2022	**Lava glass**	**Tephra glass**	**Recalculated melt**	***Uncertainty***
Eq. 13	1183°C	1193°C	1196°C	*+/- 72°C*
Eq. 16	1157°C	1172°C	1170°C	*+/- 26°C*

Table 5.2.3 Calculated temperatures for the 2022 tephra, lava, and recalculated melt.

As seen in Table 5.2.2, there is a significant difference in the estimated magma temperatures for the 2021 eruption based on which melt compositions are used. The lava glass compositions, which contain a notably larger amount of microlites, yield a much lower value than the glass in the tephra. The difference is around 40°C regardless of which equation was used. The difference in T between the lava glass and the recalculated melt is 60 – 80°C. The variations shown in the three types of melts (lava glass, tephra glass and recalculated melt) are beyond the uncertainty of equation 16. These variations are significant and show a gradually decreasing temperature from the most primitive to the least primitive compositions.

There is much less difference between the estimated magma temperatures for the 2022 eruption based on which melt compositions are used, as seen in Table 5.2.3. The values for

the tephra glass and the recalculated melt are almost identical, regardless of which equation is used. The values for the lava glass temperatures are slightly lower than those of the tephra glass and the recalculated melt. However, the differences are all within the uncertainty range for both equations and are therefore insignificant.

When compared, the temperature estimates for the lava glass in both eruptions are similar, with only a 3°C difference in the equation 16 values (1160°C for 2021 and 1157°C for 2022). The difference in tephra glass values for equation 16 is just outside of the uncertainty range, the 2021 tephra glass being 30°C warmer than the 2022 tephra glass. The pressure derived from the tephra glasses are significantly different in the two eruptions. The calculated pressure for the 2021 tephra is 4.2 kbar, which is around 13 km depth. This is similar to the pressures calculated by Halldórsson et al. (2022) for the same phase of the 2021 eruption. However, the pressure calculated for the 2022 tephra is 2.1 kbar, about 6 km depth. This suggests that the 2022 tephra equilibrated with its crystal cargo at significantly shallower depths than the 2021 tephra. The biggest difference in the temperature values is for the recalculated melt, the 2021 melt being ~70°C warmer than the 2022 one, well beyond the uncertainty range of equation 16. However, the estimated temperatures for the recalculated melt based on equation 16 aren't as reliable as those for the tephra and lava glass, due to the pressure values for the recalculated melt having a high uncertainty. But when the recalculated melt temperatures from equation 13 are compared the 2021 magma is still 40°C hotter than the 2022 magma, but well within the uncertainty range of ±72°C. The estimated pressure for the 2021 recalculated melt is 7.29 kbar, which is around 22 km depth, with an uncertainty of ±3.4 km. The estimated pressure for the 2022 recalculated melt is 1.91 kbar, which is around 6 km ±3.4 km. The 2021 magma from the fountaining phase of the eruption is therefore sourced from sub-Moho depths, while the 2022 magma from the start of the eruption is derived from the middle crust.

The reason for the insignificant difference between estimated temperatures for the melt compositions from the 2022 eruption could be the fact that there is much less microlite crystallization occurring between those samples (see Figures 4.1.4 and 4.1.5): This can be explained by the fact that the lava from 2022 spent maximum one day on the surface after emplacement and before sampling, thus it cooled very little. In contrast the lava from 2021 was on the surface for multiple days (for approximately four days) before sampling. Therefore, a significantly larger amount of microlites crystallized upon cooling within the lava in 2021 compared to the tephra which was quenched instantly as reached the surface (see Figures 4.1.1, 4.1.2 and 4.1.3). The reason for such a significant difference in calculated temperatures for the tephras could be that the magma from 2021 is sourced from a deep near-Moho reservoir, while the magma from 2022 is derived from the middle crust, where it cooled before erupting in 2022. As can be seen in Figure 5.1.1, compositionally these two melts can be derived from each other through fractional crystallization.

Judging by these results, microlite crystallization does influence the derived melt temperatures. There is little to no difference in derived temperatures for the 2022 melt compositions, where there is little to no microlite crystallization occurring between samples. In 2021 when there is significant microlite crystallization between samples, there is also a significant difference in the derived melt temperatures.

5.3 Mineral-melt equilibrium

The equilibrium compositions for ol, cpx and plag for the 2021 and 2022 lava glass, tephra glass and recalculated melt were calculated as explained in Chapter 3.7. The equilibrium compositions represent the compositional values of the minerals that crystallize from a certain melt composition.

Halldórsson et al. (2022) analyzed macrocrysts from the tephra sample of the 2021 eruption, whereas Caracciolo et al. (unpublished data) did the same with macrocrysts from the 2022 tephra sample. Their data show that the average Fo-content of ol macrocrysts was 87, the average Mg# for cpx was 86 and the average An-content for plag was 85 in the 2021 samples, whereas in 2022 the average Fo-content of ol macrocrysts was 85, the average Mg# for cpx was 85 and the average An-content for plag was 84 (Tables 5.3.1-5.3.3).

Ol	**Equilibrium Fo max**	**Equilibrium Fo min**	**Average microlite Fo-content**	**Average mpc rim Fo-content**	**Average mpc core Fo-content**	**Average macrocryst Fo-content**
2021 lava	79	75	69	71	80	-
2021 tephra	85	82	75	76	73	87
2021 recalc. melt	86	83	-	-	-	-
2022 lava	80	77	69	72	75	-
2022 tephra	82	79	74	73	75	85
2022 recalc. melt	83	81	-	-	-	-

Table 5.3.1: Max and min equilibrium Fo-content of olivine in the 2021 and 2022 lava glass, tephra glass, and recalculated melt, compared to average Fo-content of ol microlites, mpc rims and cores. Average Fo-content of macrocrysts are from Halldórsson et al. (2021) and Caracciolo et al. (unpublished).

Table 5.3.1 shows the maximum and minimum equilibrium Fo-content of ol in the 2021 and 2022 lava glass, tephra glass and recalculated melt, compared to the average Fo-content of ol microlites, mpc rims and cores.

Table 5.3.2 shows the maximum and minimum equilibrium Mg# of cpx in the 2021 and 2022 lava glass, tephra glass and recalculated melt, compared to the average Mg# of ol microlites, mpc rims and cores. It is worth it to point out that there is little variation in the

Mg# for the cpx's analyzed in this study, possibly due to only a few of them being observed in the samples.

Cpx	**Equilibrium Mg# max**	**Equilibrium Mg# min**	**Average microlite Mg#**	**Average mpc rim Mg#**	**Average mps core Mg#**	**Average macrocryst Mg#**
2021 lava	81	77	81	82	82	-
2021 tephra	86	83	81	-	-	86
2021 recalc. melt	87	85	-	-	-	-
2022 lava	82	79	80	82	83	-
2022 tephra	84	81	81	80	83	85
2022 recalc. melt	85	82	-	-	-	-

Table 5.3.2: Max and min equilibrium Mg# of clinopyroxene in the 2021 and 2022 lava glass, tephra glass, and recalculated melt, compared to the average Mg# of cpx microlites, mpc rims and cores.

Plag	**Equilibrium An-content (±5% error)**	**Average microlite An-content**	**Average mpc rim An-content**	**Average mpc core An-content**	**Average macrocryst An-content**
2021 lava	74	75	-	-	-
2021 tephra	81	76	77	75	85
2021 recalc. melt	81	-	-	-	-
2022 lava	76	73	79	81	-
2022 tephra	79	79	78	78	84
2022 recalc. melt	81	-	-	-	-

Table 5.3.3: Equilibrium An-content of plagioclase in the 2021 and 2022 lava glass, tephra glass, and recalculated melt, compared to the average An-content of plag microlites, mpc rims and cores.

Table 5.3.3 shows the maximum and minimum equilibrium An-content of plag in the 2021 and 2022 lava glass, tephra glass and recalculated melt, compared to the average An-content of plag microlites, mpc rims and cores.

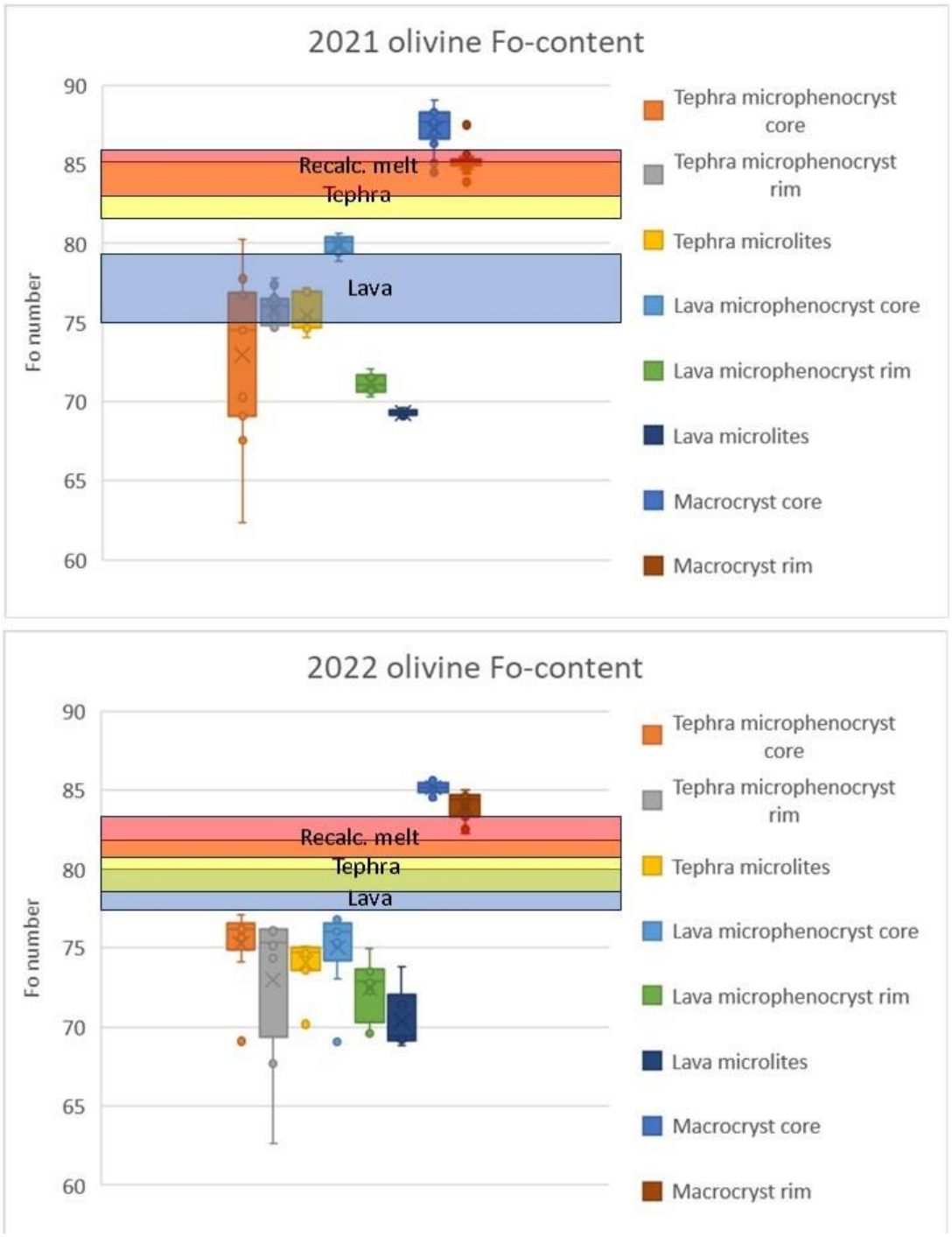

Figure 5.3.1: Equilibrium compositional ranges of olivine for lava glass, tephra glass and recalculated melt, compared to the tephra and lava mpc cores, rims and microlites, as well as macrocryst core and rim compositions as calculated by Halldórsson et al. (2022) for 2021 and Alberto Caracciolo (unpublished data) for 2022.

Figures 5.3.1-5.3.3 show the equilibrium compositional ranges of ol, cpx and plag respectively, with lava glass, tephra glass and recalculated melt, compared to the tephra and lava mpc cores, rims and microlites, as well as macrocryst core and rim compositions as calculated by Halldórsson et al. (2022) for 2021 and Caracciolo et al. (unpublished data) for 2022. Cpx and plag microlites, which should be the last products in the lava, are generally in equilibrium with the lava glass, except for plag microlites in the 2022 lava. This is not the case for the ol microlites, which might be due to heterogeneity within the melt: there is a higher Fe-content in the glass in the vicinity of ol microlites relative to other areas within the glass (Appendix B, shows decreased Mg-content around ol microlites). All points analysed in the tephra and lava glass were in areas scarce of microlites, and therefore the ol microlites might be in equilibrium with the more Fe-rich melt. The ol microlites in the lava not being in equilibrium with the lava glass could also be due to the Kd value used to calculate the equilibrium compositions being a bit high for these melt compositions.

In both eruptions the mineral compositions in the lava gradually evolve from mpc core, to rim, to microlites. However, the tephra mineral compositions do not show the same systematic variations. This might be due to the fast cooling of the tephra. The lava cools slower, providing the possibility of the development of various compositional ranges.

In 2021, there is a clear difference between the mineral compositions which are supposed to be in equilibrium with the lava glass and tephra glass, since there is a large difference in the glass compositions. Some cpx and plag microlites in the lava fall within the equilibrium range with the lava, but many are more evolved. The microlites in equilibrium with the lava glass crystallized on or close to the surface. Many microlites and mpc's in the tephra also show equilibrium composition with the lava glass. However, these minerals could not have formed in equilibrium with the lava glass since the tephra quenched as soon as it erupted. This discrepancy could be because the small minerals do not represent equilibrium, but rather they are crystallizing extremely fast in disequilibrium, perhaps during uplift in the conduit.

In 2022, the glass compositions are quite similar in tephra and lava as mentioned before. In these samples the equilibrium ranges strongly overlap. Lava cpx and plag microlites are still more likely to be in equilibrium with the lava glass than with the tephra glass, which indicated that these microlites crystallized on the surface. However, mpc's of the same minerals are more likely to crystallize from the tephra glass, which indicates that they crystallized in the mid-crust. The ol seem to be too evolved to be in equilibrium with any of the melts. As mentioned above, this might be due to the ol microlites being associated with the more Fe-rich parts of the melt or the high Kd value used in the calculations.

Regarding the macrocrysts, for both eruptions the rims of all the macrocrysts are generally in equilibrium with the recalculated melts, meaning the outer parts of these minerals formed before microlite crystallization ensued. However, the macrocryst cores of ol and plag are not in equilibrium with any of the melt compositions, meaning they formed from a more primitive melt than the ones reproduced with these calculations. The only exception to this are some cpxs, which are in some cases in equilibrium with the recalculated melts.

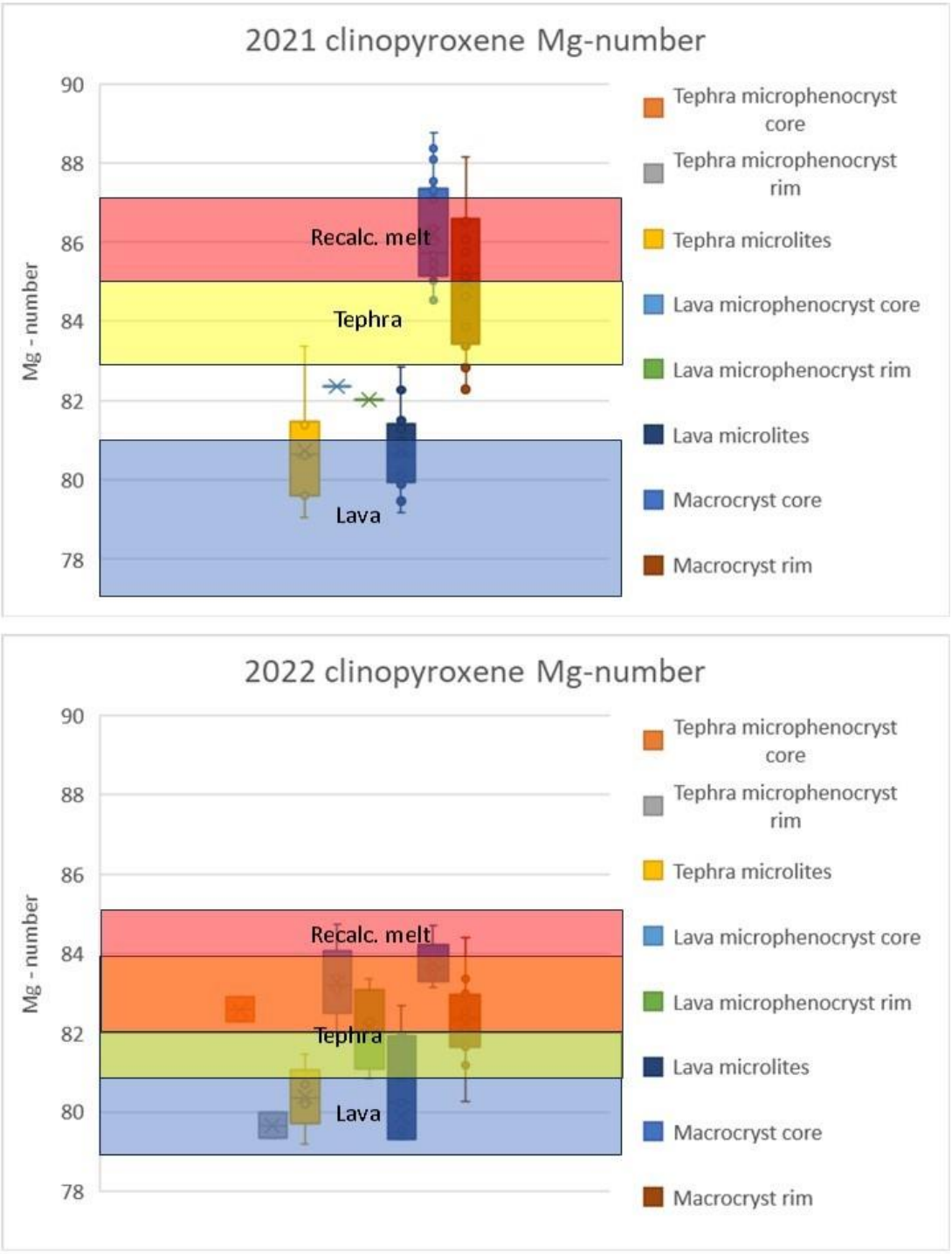

Figure 5.3.2: Equilibrium compositional ranges of clinopyroxene for lava glass, tephra glass and recalculated melt, compared to the tephra and lava mpc cores, rims and microlites, as well as macrocryst core and rim compositions as calculated by Halldórsson et al. (2022) for 2021 and Alberto Caracciolo (unpublished data) for 2022.

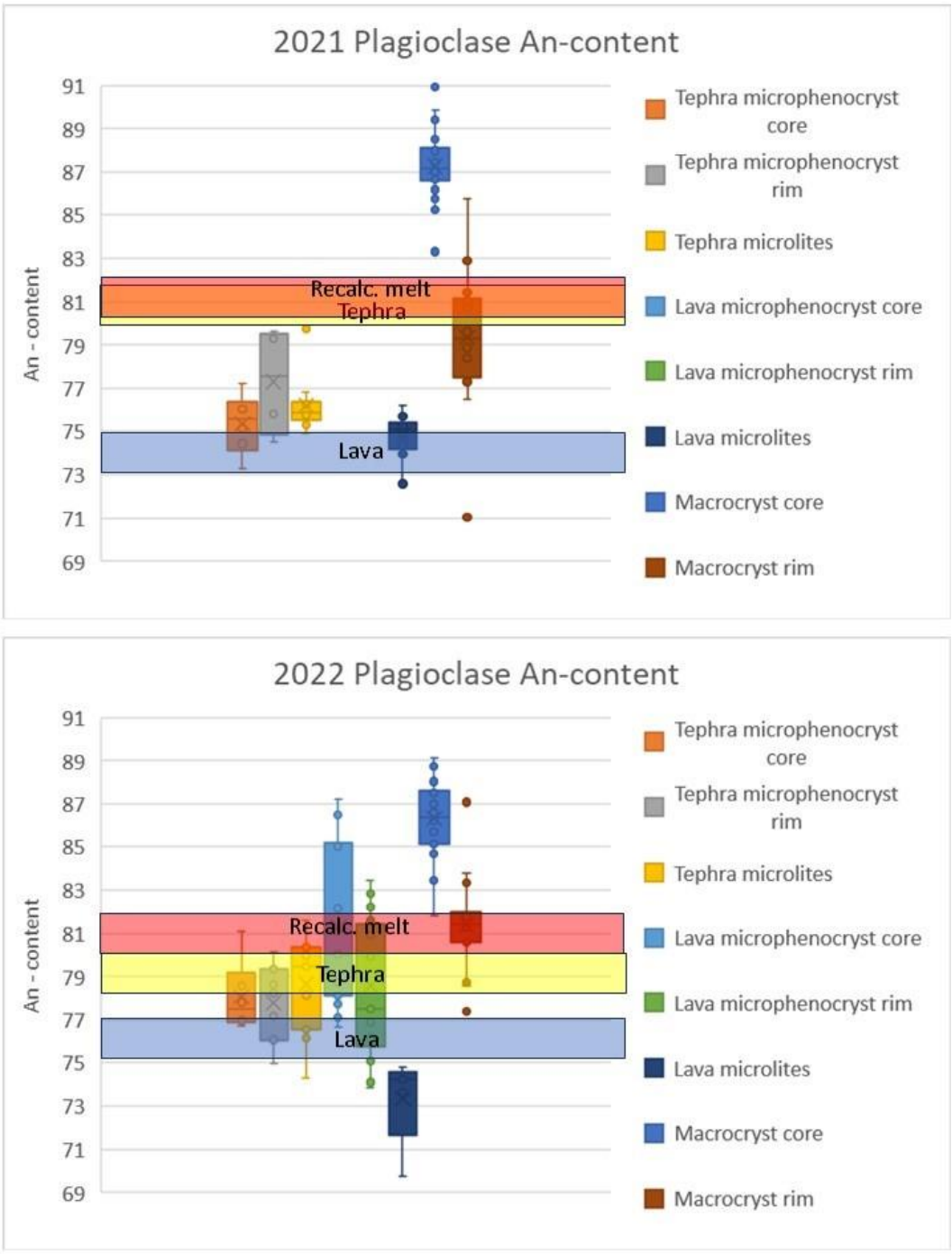

Figure 5.3.3: Equilibrium compositional ranges of plagioclase for lava glass, tephra glass and recalculated melt, compared to the tephra and lava mpc cores, rims and microlites, as well as macrocryst core and rim compositions as calculated by Halldórsson et al. (2022) for 2021 and Alberto Caracciolo (unpublished data) for 2022.

6 Conclusion

In this work I have studied the effect of microlite crystallization on the melt composition and derived temperatures in the 2021 and 2022 Fagradalsfjall eruptions. Major conclusions are:

- There is a big difference between the crystallinities of the 2021 and 2022 samples. The 2021 tephra is barely crystalline while the lava contains abundant microlites. In contrast, the microlite crystallinities of the 2022 tephra and lava are very similar. The 2022 samples contain a much larger ratio of cpx to ol (5 cpx/1 ol), compared to the 2021 samples, where the ratio is about 1 cpx/1 ol. The ratio of plag to ol+cpx is similar in samples from both 2021 and 2022.

- The 2021 lava glass is significantly more evolved than the 2021 tephra glass, which is more evolved than the 2021 recalculated melt. This is not the same for the 2022 eruption, where the lava glass is only slightly more evolved than the tephra glass, which is only slightly more evolved than the recalculated melt. There is therefore a significant gradual change in the 2021 compositions while this change in the 2022 compositions is less significant. The 2022 magma can be derived from the 2021 magma through fractional crystallization.

- Cpx and plag lava microlites are generally in equilibrium with the lava glass, while the same does not go for ol microlites in the lava. Ol, cpx and plag microlites within the tephra are generally not in equilibrium with the tephra glass, which might represent disequilibrium growth. Cpx and plag lava mpc's are often in equilibrium with the tephra from the same eruption. Ol mpc's are in disequilibrium with all melt compositions. Macrocryst rims for all minerals are usually in equilibrium with the recalculated melt, while the macrocrysts cores are most often in disequilibrium with all melt compositions.

- There is a significant difference between calculated temperatures for the 2021 melt compositions. The lava glass yields a temperature value of 1160°C, the tephra glass 1202°C and the recalculated melt 1243°C ± 26°C. The difference between the lava and tephra temperatures is likely due to the large amount of microlites that crystallized between tephra (10% microlites) and lava (36% microlites) samples, while the lava was flowing on the surface for several days.

- There is no significant difference between calculated temperatures for the 2022 melt compositions. The lava glass yields a temperature value of 1157°C, the tephra glass 1172°C and the recalculated melt 1170°C ± 26°C. This is likely because little to no microlite crystallization occurred between samples as the lava was sampled within a day since it was emplaced on the surface.

References

Applegarth, L.J., Tuffen, H., James, M.R., Pinkerton, H., Cashman, K.V., (2013). Direct observations of degassing-induced crystallization in basalts. Geology 41, 243–246. https://doi.org/10.1130/G33641.1.

Baxter, R.J.M., Maclennan, J., Neave, D.A., Thordarson, T. (2023). Depth of magma storage under Iceland controlled by magma fluxes. Geochem. Geophys. Geosyst., 24 (7). Article e2022GC010811.

Bédard, J.H. (2010). Parameterization of the Fe=Mg exchange coefficient (Kd) between clinopyroxene and silicate melts, Chemical Geology, Volume 274, Issues 3–4, Pages 169-176, ISSN 0009-2541, https://doi.org/10.1016/j.chemgeo.2010.04.003.

Binderman, I.N., Deegan, F.M., Troll, V.R., Thordarson, T., Höskuldsson, Á., Moreland, W.M., Zorn, E.U., Shevchenko, A. V. and Walter, T.R. (2022). Diverse mantle components with invariant oxygen isotopes in the 2021 Fagradalsfjall eruption, Iceland. Nature Communications, 13(3737). https://doi.org/10.1038/s41467-022-31348-7

Caracciolo, A., Bali, E., Halldórsson, S.A., Guðfinnsson, G.H., Kahl, M., Þórðardóttir, I., Pálmadóttir, G.L., Silvestri, V. (2023). Magma plumbing architectures and timescales of magmatic processes during historical magmatism on the Reykjanes Peninsula, Iceland. Earth and Planetary Science Letters. Volume 621. 118378. https://doi.org/10.1016/j.epsl.2023.118378.

Cashman, K.V., (1993)., Relationship between plagioclase crystallization and cooling rate in basaltic melts: Contributions to Mineralogy and Petrology, v. 113, p. 126–142, doi:10.1007/BF00320836.

Cimarelli, C., Di Traglia, F., Taddeucci, J., (2010). Basaltic scoria textures from a zoned conduit as precursors to violent Strombolian activity. Geology 38, 439–442. https://doi.org/10.1130/G30720.1.

Deardorff, N., Cashman, K. (2017). Rapid crystallization during recycling of basaltic andesite tephra: timescales determined by reheating experiments. Sci Rep 7, 46364. https://doi.org/10.1038/srep46364.

Danyushevsky, L. V., and P. Plechov. (2011). Petrolog3: Integrated software for modeling crystallization processes, Geochem. Geophys. Geosyst., 12, Q07021, doi:10.1029/2011GC003516.

Flovenz, O., Wang, R., Hersir, G., Dahm, T., Hainzl, S., Vassileva, M., Drouin, V., Heimann, S., Isken, M., Gudnason, E., Ágústsson, K., Agustsdottir, T., Horalek, J., Motagh, M., Walter, T. R., Rivalta, E., Jousset, P., Krawczyk, C., & Milkereit, C. (2022). Cyclical geothermal unrest as a precursor to Iceland's 2021 Fagradalsfjall eruption. Nature Geoscience, 15. https://doi.org/10.1038/s41561-022-00930-5

Gudmundsson, A. (1986). Mechanical aspects of postglacial volcanism and tectonics of the Reykjanes Peninsula, southwest Iceland. Journal of Geophysical Research: Solid

Earth, 91(B12), 12711-12721. https://doi.org/https://doi.org/10.1029/JB091iB12p12711

Guilbaud, M.-N., Blake, S., Thordarson, T., and Self, S., (2007)., Role of syn-eruptive cooling and degassing on textures of lavas from the AD 1783-1784 Laki eruption, South Iceland: Journal of Petrology, v. 48, p. 1265–1294, doi: 10.1093/petrology/egm017.

Haldeman, M.R. (2018). Degassing-induced crystallization in subaerial and submarine basaltic lavas. Master's thesis, Faculty of Earth Sciences, University of Iceland, Reykjavík.

Halldórsson, S. A., Marshall, E. W., Caracciolo, A., Matthews, S., Bali, E., Rasmussen, M. B., Ranta, E., Robin, J. G., Guðfinnsson, G. H., Sigmarsson, O., Maclennan, J., Jackson, M. G., Whitehouse, M. J., Jeon, H., van der Meer, Q. H. A., Mibei, G. K., Kalliokoski, M. H., Repczynska, M. M., Rúnarsdóttir, R. H., . . . Stefánsson, A. (2022). Rapid shifting of a deep magmatic source at Fagradalsfjall volcano, Iceland. Nature, 609(7927), 529-534. https://doi.org/10.1038/s41586-022-04981-x

Hartley, M.E., E. Bali, E., J. Maclennan, J., D.A. Neave, D.A., S.A. Halldórsson, S.A. (2018). Melt inclusion constraints on petrogenesis of the 2014–2015 Holuhraun eruption, Iceland. Contrib. Mineral. Petrol., 173 (2018), pp. 1-23, 10.1007/s00410-017-1435-0.

Helz & Thornber (1987), Geothermometry of Kilauea Iki lava lake, Hawaii. Bulletin of Volcanology, 49 bls. 651 – 668.

Jakobsson, S. P., Jónsson, J., & Shido, F. (1978). Petrology of the Western Reykjanes Peninsula, Iceland. Journal of Petrology, 19(4), 669-705. https://doi.org/10.1093/petrology/19.4.669

Jakobsson, S., Jónasson, K., & Sigurdsson, I. (2008). The three igneous rock series of Iceland. Jokull, 58, 117-138.

Lange, R. A., Carmichael, I.S.E. (1987). Densities of Na2O-K2O-CaO-MgO-FeO-Fe2O3-Al2O3-TiO2-SiO2 liquids: New measurements and derived partial molar properties, Geochimica et Cosmochimica Acta, Volume 51, Issue 11, Pages 2931-2946, ISSN 0016-7037, https://doi.org/10.1016/0016-7037(87)90368-1.

Lesher, C.E., Cashman, K. V., and Mayfield, J.D., (1999)., Kinetic controls on crystallization of Tertiary North Atlantic basalt and implications for the emplacement and cooling history of lava at Site 989, Southeast Greenland rifted margin, in Larsen, H.C., Duncan, R.A., Allan, J.F., and Brooks, K. eds., Proceedings of the Ocean Drilling Program: Scientific Results, College Station, Texas, v. 163, p. 135–148, doi: 10.2973/odp.proc.sr.163.115.1999.

Lofgren, G., 1980, Experimental studies on the dynamic crystallization of silicate melts, in Hargreaves, R.B., ed., Physics of Magmatic Processes: New Jersey, Princeton University Press, p. 487–551.

Lofgren, G.E., (1974)., An experimental study of plagioclase crystal morphology: Isothermal crystallization: American Journal of Science, v. 274, p. 243–273, doi: 10.2475/ajs.274.3.243.

Marshall, E.W., Caracciolo, A., Ranta, E., Sigmarsson, O., Bali, E., Rasmussen, M.B., Matthews, S., Gunnarsson-Robin, J., Hallsórsson, S.A., Guðfinnsson, G.H., Lowe, N. (2023). Geochemical evolution of the 2021 and 2022 Fagradalsfjall eruptions. Oral presentation. https://conf.goldschmidt.info/goldschmidt/2023/meetingapp.cgi/Paper/18545.

Martel, C., Ali, A.R., Poussineau, S., Gourgaud, A., and Pichavant, M., (2006)., Basalt-inherited microlites in silicic magmas: Evidence from Mount Pelée (Martinique, French West Indies): Geology, v. 34, p. 905–908, doi: 10.1130/G22672A.1.

Neave, D., & Putirka, K. (2017). A new clinopyroxene-liquid barometer, and implications for magma storage pressures under Icelandic rift zones. American Mineralogist, 102, 777-794. https://doi.org/10.2138/am-2017-5968

Pedersen, G. B. M., Belart, J. M. C., Óskarsson, B. V., Gudmundsson, M. T., Gies, N., Högnadóttir, T., et al. (2022). Volume, effusion rate, and lava transport during the 2021 Fagradalsfjall eruption: Results from near real-time photogrammetric monitoring. Geophysical Research Letters, 49, e2021GL097125. https://doi.org/10.1029/2021GL097125.

Putirka, K. D. (2008). Thermometers and Barometers for Volcanic Systems. Reviews in Mineralogy and Geochemistry, 69(1), 61-120. https://doi.org/10.2138/rmg.2008.69.3

Sæmundsson, K., & Sigurgeirsson, M. Á. (2013). Reykjanesskagi. In Sólnes, Júlíus (Ed.), Náttúruvá á Íslandi. Eldgos og Jarðskjálftar: Viðlagatrygging Íslands/Háskólaútgáfan.

Sæmundsson, K., Sigurgeirsson, M. Á., & Friðleifsson, G. Ó. (2020). Geology and structure of the Reykjanes volcanic system, Iceland. Journal of Volcanology and Geothermal Research, 391, 106501. https://doi.org/https://doi.org/10.1016/j.jvolgeores.2018.11.022

Sæmundsson, K. (1979). Outline of the geology of Iceland. Jokull, 29.

Schilling, J.G. (1973). Iceland Mantle Plume: Geochemical Study of Reykjanes Ridge. Nature, 242, 565-571. https://doi.org/10.1038/242565a0

Sigmarsson, O., Keiding, J. K. (2010). Geothermobarometry of the 2010 Eyjafjallajökull eruption: New constraints on Icelandic magma plumbing systems. Journal of Geophysical Research, 117.

Sigmundsson, F., Parks, M., Hooper, A., Geirsson, H., Vogfjörd, K. S., Drouin, V., Ófeigsson, B. G., Hreinsdóttir, S., Hjaltadóttir, S., Jónsdóttir, K., Einarsson, P., Barsotti, S., Horálek, J., & Ágústsdóttir, T. (2022). Deformation and seismicity decline before the 2021 Fagradalsfjall eruption. Nature, 609(7927), 523-528. https://doi.org/10.1038/s41586-022-05083-4

Szramek, L., Gardner, J.E., and Hort, M., (2010)., Cooling-induced crystallization of microlite crystals in two basaltic pumice clasts: American Mineralogist, v. 95, p. 503–509, doi: 10.2138/am.2010.3270.

Thordarson, T., Self, S., Óskarsson, N., and Hulsebosch, T., (1996)., Sulfur, chlorine, and fluorine degassing and atmospheric loading by the 1783-1784 AD Laki (Skaftar Fires) eruption in Iceland: Bulletin of Volcanology, v. 58, p. 205–225, doi: 10.1007/s004450050136.

Yang, H.J., Kinzler, R.J., and Grove, T.L. (1996). Experiments and models of anhydrous, basaltic olivine-plagioclase-augite saturated melts from 0.001 to 10 kbar. Contrib. Mineral. Petrol., 124 (1996), pp. 1-18, 10.1007/s004100050169.

Appendix A

EPMA-analyses of olivine, plagioclase feldspar, clinopyroxene, and glass: representative compositions.

Olivine Compositions - in Weight Percent										
	SiO2	TiO2	Al2O3	FeOt	MnO	MgO	CaO	Na2O	K2O	Cr2O3
2021 tephra microlite 1	39.23	0.03	0.10	14.71	0.19	44.37	0.49	0.00	0.00	0.04
2021 tephra microlite 2	39.35	0.05	0.05	13.39	0.21	45.34	0.45	0.00	0.00	0.09
2021 tephra microlite 3	39.53	0.03	0.10	15.36	0.18	43.91	0.43	0.00	0.00	0.07
2021 tephra core 1	38.41	0.06	0.09	17.70	0.26	41.95	0.43	0.00	0.00	0.08
2021 tephra rim 1	39.13	0.04	0.27	14.78	0.27	44.13	0.52	0.00	0.00	0.10
2021 tephra core 2	38.61	0.04	0.17	19.42	0.33	40.39	0.53	0.00	0.00	0.03
2021 tephra rim 2	39.14	0.05	0.06	15.02	0.16	44.46	0.44	0.00	0.00	0.04
2021 tephra core 3	39.93	0.01	0.04	13.83	0.20	45.65	0.31	0.00	0.00	0.08
2021 tephra rim 3	40.14	0.02	0.08	13.41	0.23	45.89	0.39	0.00	0.00	0.07
2021 lava microlite 1	38.92	0.04	0.08	18.45	0.33	41.31	0.44	0.00	0.00	0.04
2021 lava microlite 2	38.91	0.02	0.06	18.40	0.32	41.22	0.40	0.00	0.00	0.03
2021 lava microlite 3	38.96	0.03	0.09	18.39	0.33	41.21	0.42	0.00	0.00	0.07
2021 lava core 1	40.35	0.00	0.04	12.52	0.19	46.68	0.32	0.00	0.00	0.09
2021 lava rim 1	39.22	0.03	0.04	17.50	0.23	42.20	0.37	0.00	0.00	0.06
2021 lava core 2	40.45	0.02	0.05	11.78	0.19	47.10	0.31	0.00	0.00	0.03
2021 lava rim 2	39.46	0.02	0.03	17.01	0.31	42.87	0.35	0.00	0.00	0.04
2021 lava core 3	40.45	0.00	0.06	11.62	0.17	47.63	0.30	0.00	0.00	0.06
2021 lava rim 3	39.47	0.02	0.06	16.70	0.27	43.08	0.33	0.00	0.00	0.05
2022 tephra microlite 1	39.76	0.05	0.08	15.66	0.25	43.61	0.47	0.00	0.00	0.07
2022 tephra microlite 2	39.54	0.04	0.08	14.84	0.25	44.54	0.49	0.00	0.00	0.05
2022 tephra microlite 3	39.58	0.02	0.11	14.75	0.23	44.52	0.47	0.00	0.00	0.17
2022 tephra core 1	40.06	0.01	0.05	14.46	0.23	44.94	0.35	0.00	0.00	0.07
2022 tephra rim 1	39.90	0.05	0.05	14.48	0.24	44.85	0.37	0.00	0.00	0.05
2022 tephra core 2	39.97	0.00	0.05	13.90	0.20	45.46	0.32	0.00	0.00	0.08
2022 tephra rim 2	40.12	0.01	0.04	14.16	0.25	45.43	0.38	0.00	0.00	0.02
2022 tephra core 3	39.96	0.01	0.04	14.35	0.22	44.97	0.34	0.00	0.00	0.04
2022 tephra rim 3	39.96	0.03	0.06	14.11	0.24	45.16	0.39	0.00	0.00	0.03
2022 lava microlite 1	38.83	0.03	0.03	18.62	0.29	41.80	0.47	0.00	0.00	0.07
2022 lava microlite 2	39.56	0.03	0.05	15.71	0.25	44.20	0.42	0.00	0.00	0.04
2022 lava microlite 3	38.93	0.05	0.06	18.35	0.27	41.74	0.51	0.00	0.00	0.05
2022 lava core 1	40.11	0.02	0.06	13.84	0.18	45.80	0.32	0.00	0.00	0.05
2022 lava rim 1	39.42	0.03	0.05	16.11	0.22	43.55	0.41	0.00	0.00	0.04
2022 lava core 2	40.21	0.02	0.06	13.79	0.27	45.71	0.33	0.00	0.00	0.06
2022 lava rim 2	39.25	0.03	0.05	18.21	0.28	41.71	0.43	0.00	0.00	0.04
2022 lava core 3	40.02	0.00	0.06	14.11	0.26	45.55	0.35	0.00	0.00	0.06
2022 lava rim 3	39.79	0.02	0.03	15.85	0.22	44.35	0.37	0.00	0.00	0.04

Feldspar Compositions - in Weight Percent										
	SiO2	TiO2	Al2O3	FeOt	MnO	MgO	CaO	Na2O	K2O	Cr2O3
2021 tephra microlite 1	49.34	0.13	31.04	1.13	0.01	0.73	15.02	2.58	0.09	0.00
2021 tephra microlite 2	48.84	0.04	32.09	0.87	0.02	0.30	15.17	2.63	0.09	0.00
2021 tephra microlite 3	48.78	0.04	31.99	0.75	0.02	0.31	15.24	2.63	0.07	0.00
2021 tephra core 1	48.97	0.05	31.87	0.89	0.00	0.16	15.00	2.81	0.05	0.00
2021 tephra rim 1	47.99	0.05	32.25	1.19	0.01	0.30	15.81	2.20	0.06	0.00
2021 tephra core 2	48.92	0.06	32.18	0.77	0.01	0.31	15.46	2.48	0.05	0.00
2021 tephra rim 2	49.76	0.07	31.91	0.83	0.00	0.22	14.99	2.78	0.08	0.00
2021 tephra core 3	44.05	0.00	36.73	0.39	0.01	0.06	18.87	0.45	0.01	0.00
2021 tephra rim 3	48.54	0.03	33.18	0.70	0.02	0.25	15.90	2.26	0.05	0.00
2021 lava microlite 1	48.87	0.07	32.12	1.11	0.02	0.25	15.16	2.65	0.09	0.00
2021 lava microlite 2	49.19	0.06	32.14	0.89	0.02	0.23	15.00	2.66	0.09	0.00
2021 lava microlite 3	49.75	0.06	31.74	1.02	0.02	0.28	14.84	2.69	0.09	0.00
2021 lava microlite 4	49.26	0.07	31.79	0.92	0.01	0.27	15.03	2.67	0.09	0.00
2022 tephra microlite 1	48.46	0.03	33.36	0.67	0.02	0.25	16.02	2.07	0.07	0.00
2022 tephra microlite 2	49.03	0.03	33.08	0.69	0.02	0.29	15.61	2.37	0.07	0.00
2022 tephra microlite 3	49.55	0.06	31.59	0.86	0.00	0.32	14.81	2.77	0.09	0.00
2022 tephra core 1	49.38	0.07	32.75	0.55	0.00	0.31	15.28	2.51	0.08	0.00
2022 tephra rim 1	49.53	0.03	32.26	0.88	0.00	0.35	14.89	2.69	0.09	0.00
2022 tephra core 2	48.83	0.06	32.84	0.66	0.01	0.33	15.61	2.41	0.07	0.00
2022 tephra rim 2	48.34	0.04	32.64	0.72	0.00	0.28	15.63	2.31	0.06	0.00
2022 tephra core 3	49.17	0.05	31.95	0.67	0.01	0.32	15.36	2.49	0.08	0.00
2022 tephra rim 3	48.60	0.07	31.91	0.77	0.04	0.33	15.43	2.48	0.07	0.00
2022 lava microlite 1	50.12	0.07	31.85	0.85	0.02	0.31	14.71	2.74	0.10	0.00
2022 lava microlite 2	50.18	0.07	31.86	0.80	0.00	0.29	14.67	2.84	0.10	0.00
2022 lava microlite 3	49.90	0.03	31.27	0.82	0.00	0.30	14.82	2.78	0.10	0.00
2022 lava core 1	49.03	0.05	32.36	0.63	0.02	0.29	15.56	2.50	0.08	0.00
2022 lava rim 1	49.16	0.03	32.55	0.76	0.00	0.27	15.55	2.44	0.07	0.00
2022 lava core 2	48.82	0.06	32.87	0.67	0.01	0.28	15.57	2.42	0.07	0.00
2022 lava rim 2	49.78	0.06	32.03	0.84	0.02	0.29	14.84	2.80	0.11	0.00
2022 lava core 3	48.44	0.03	32.61	0.58	0.01	0.25	15.57	2.36	0.07	0.00
2022 lava rim 3	48.80	0.04	31.91	0.86	0.01	0.30	15.32	2.45	0.07	0.00

Clinopyroxene Compositions - in Weight Percent										
	SiO2	TiO2	Al2O3	FeOt	MnO	MgO	CaO	Na2O	K2O	Cr2O3
2021 tephra microlite 1	50.23	0.98	6.09	6.97	0.13	16.27	17.70	0.19	0.00	0.48
2021 tephra microlite 2	49.46	1.04	7.30	7.64	0.16	16.81	17.27	0.20	0.00	0.47
2021 tephra microlite 3	51.74	0.68	4.58	6.00	0.14	16.87	19.31	0.18	0.00	0.91
2021 lava microlite 1	50.87	0.85	4.41	6.79	0.17	15.88	20.08	0.22	0.00	0.69
2021 lava microlite 2	51.64	0.54	2.96	6.77	0.17	16.49	20.28	0.21	0.00	0.41
2021 lava microlite 3	51.11	0.67	4.36	6.15	0.15	16.67	19.74	0.18	0.00	1.22
2021 lava core 1	53.06	0.40	1.94	6.96	0.22	18.23	18.51	0.16	0.00	0.53
2021 lava rim 1	50.77	0.79	4.09	6.23	0.15	15.97	20.36	0.21	0.00	0.99
2022 tephra microlite 1	50.77	1.27	5.38	6.70	0.17	15.24	20.43	0.22	0.00	0.57
2022 tephra microlite 2	52.82	0.70	3.65	7.32	0.18	18.05	16.97	0.16	0.00	0.72
2022 tephra microlite 3	50.84	1.07	5.68	6.73	0.15	15.77	19.68	0.22	0.00	0.99
2022 tephra core 1	54.21	0.44	2.41	7.19	0.22	19.55	16.21	0.11	0.00	0.58
2022 tephra rim 1	51.46	1.12	4.87	6.86	0.16	15.39	20.57	0.21	0.00	0.41
2022 tephra core 2	53.99	0.52	2.31	7.14	0.18	18.58	17.71	0.11	0.00	0.21
2022 tephra rim 2	51.66	1.05	4.87	7.37	0.17	15.88	19.75	0.19	0.00	0.27
2022 lava microlite 1	53.40	0.53	2.57	7.04	0.18	16.71	20.40	0.18	0.00	0.26
2022 lava microlite 2	52.07	0.85	4.45	6.45	0.15	16.40	19.73	0.22	0.00	0.78
2022 lava microlite 3	51.78	0.80	4.72	7.61	0.20	17.35	17.74	0.21	0.00	0.53
2022 lava core 1	53.79	0.44	2.64	6.70	0.18	18.87	18.10	0.15	0.00	0.34
2022 lava rim 1	50.69	0.96	5.78	6.19	0.15	15.70	20.18	0.20	0.00	1.21
2022 lava core 2	53.02	0.55	3.65	6.58	0.17	18.26	18.30	0.15	0.00	0.46
2022 lava rim 2	50.36	1.11	6.15	6.57	0.15	15.56	20.10	0.23	0.00	0.84
2022 lava core 3	53.98	0.40	2.40	5.93	0.16	18.45	18.95	0.13	0.00	0.80
2022 lava rim 3	50.94	0.73	5.00	5.68	0.15	15.98	20.96	0.21	0.00	1.47

Liquid (Glass) Composition - in Weight Percent											
	SiO2	TiO2	Al2O3	FeOt	MnO	MgO	CaO	Na2O	K2O	Cr2O3	P2O5
2021 tephra point 1	49.30	1.23	15.28	9.96	0.19	8.22	12.92	1.96	0.34	0.00	0.21
2021 tephra point 2	49.14	1.19	15.50	9.74	0.17	8.58	12.72	1.93	0.31	0.00	0.20
2021 tephra point 3	49.41	1.27	15.00	9.83	0.17	8.28	12.93	1.95	0.32	0.00	0.19
2021 tephra average	49.32	1.22	15.22	9.91	0.17	8.37	12.91	1.98	0.33	0.00	0.19
2021 lava point 1	50.06	1.64	13.61	12.31	0.24	6.93	11.92	2.13	0.40	0.00	0.14
2021 lava point 2	49.80	1.61	13.61	12.42	0.24	6.81	11.88	2.10	0.40	0.00	0.24
2021 lava point 3	49.94	1.66	13.52	12.22	0.22	6.99	12.06	1.99	0.43	0.00	0.22
2021 lava average	49.95	1.65	13.12	12.22	0.22	6.79	11.79	2.03	0.41	0.00	0.20
2022 tephra point 1	49.70	1.44	14.47	11.11	0.21	7.45	12.98	1.99	0.42	0.00	0.20
2022 tephra point 2	49.98	1.33	14.83	10.49	0.20	7.74	13.08	2.10	0.39	0.00	0.15
2022 tephra point 3	49.75	1.40	14.82	10.46	0.18	7.68	12.98	2.01	0.37	0.00	0.18
2022 tephra average	49.76	1.39	14.67	10.62	0.19	7.57	13.04	2.03	0.40	0.00	0.19
2022 lava point 1	49.55	1.65	14.01	11.84	0.21	7.15	12.65	2.11	0.48	0.00	0.24
2022 lava point 2	49.93	1.64	14.15	11.67	0.21	7.12	12.70	2.15	0.42	0.00	0.28
2022 lava point 3	49.57	1.59	14.18	11.70	0.22	7.28	12.69	2.17	0.46	0.00	0.26
2022 lava average	49.67	1.63	14.08	11.70	0.20	7.19	12.67	2.15	0.46	0.00	0.25

Appendix B

WDS element maps of Mg and Ca from lava samples.

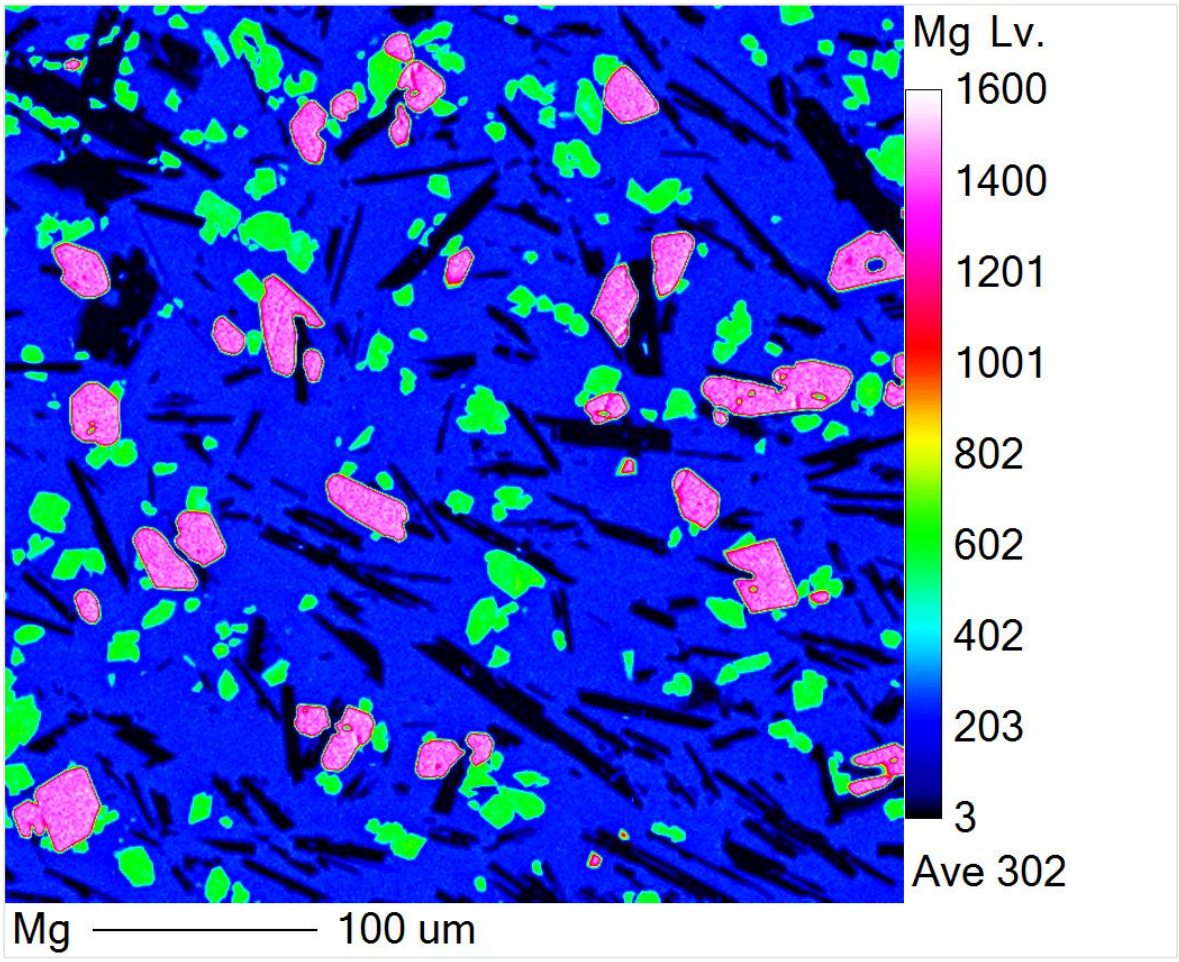

Mg map of 2021 lava groundmass. In the order of increasing Mg-content: black-plagioclase, blue-silicate glass, green-clinopyroxene, pink-olivine.

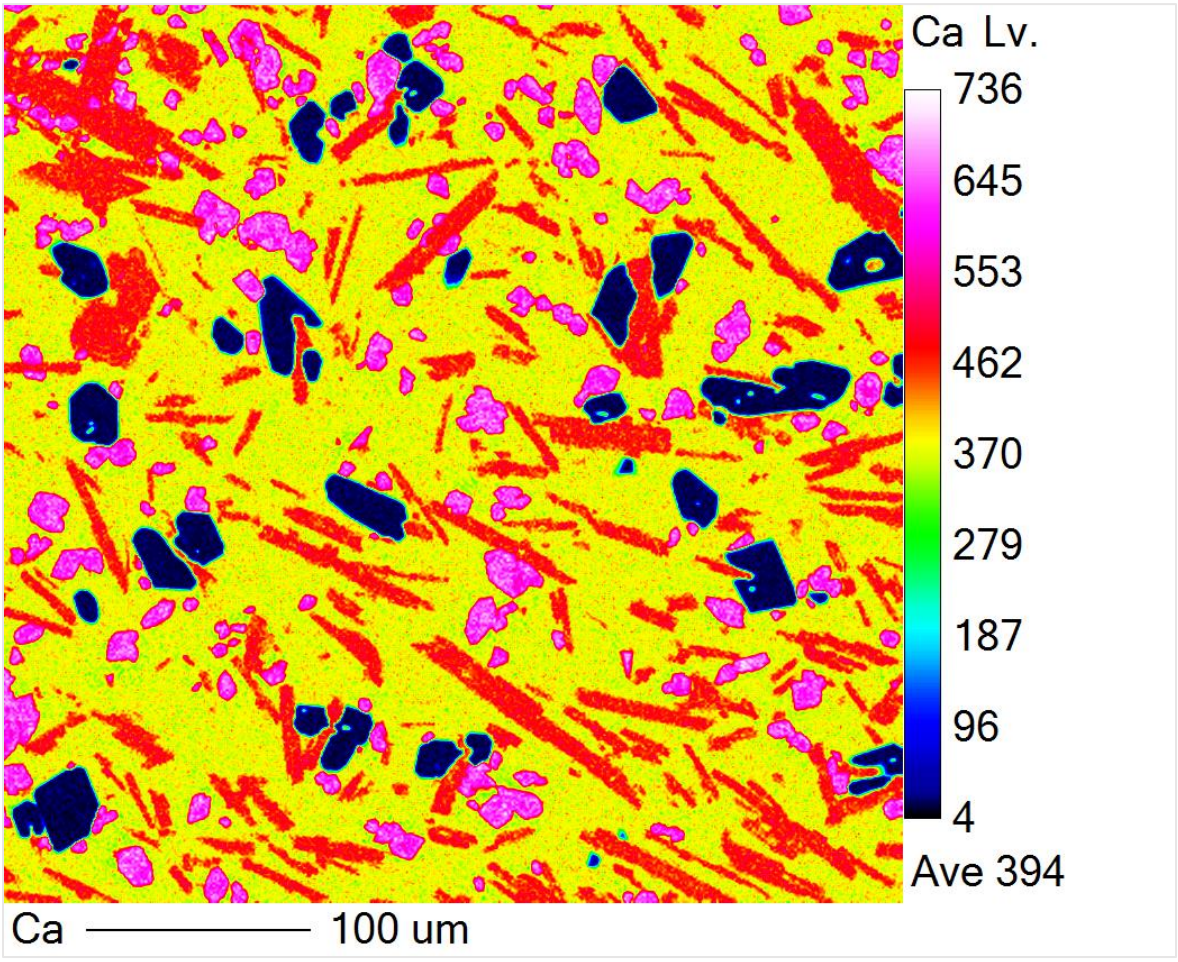

Ca map of 2021 lava groundmass. In the order of increasing Ca-content: black-olivine, yellow-silicate glass, pink-clinopyroxene, red-plagioclase.

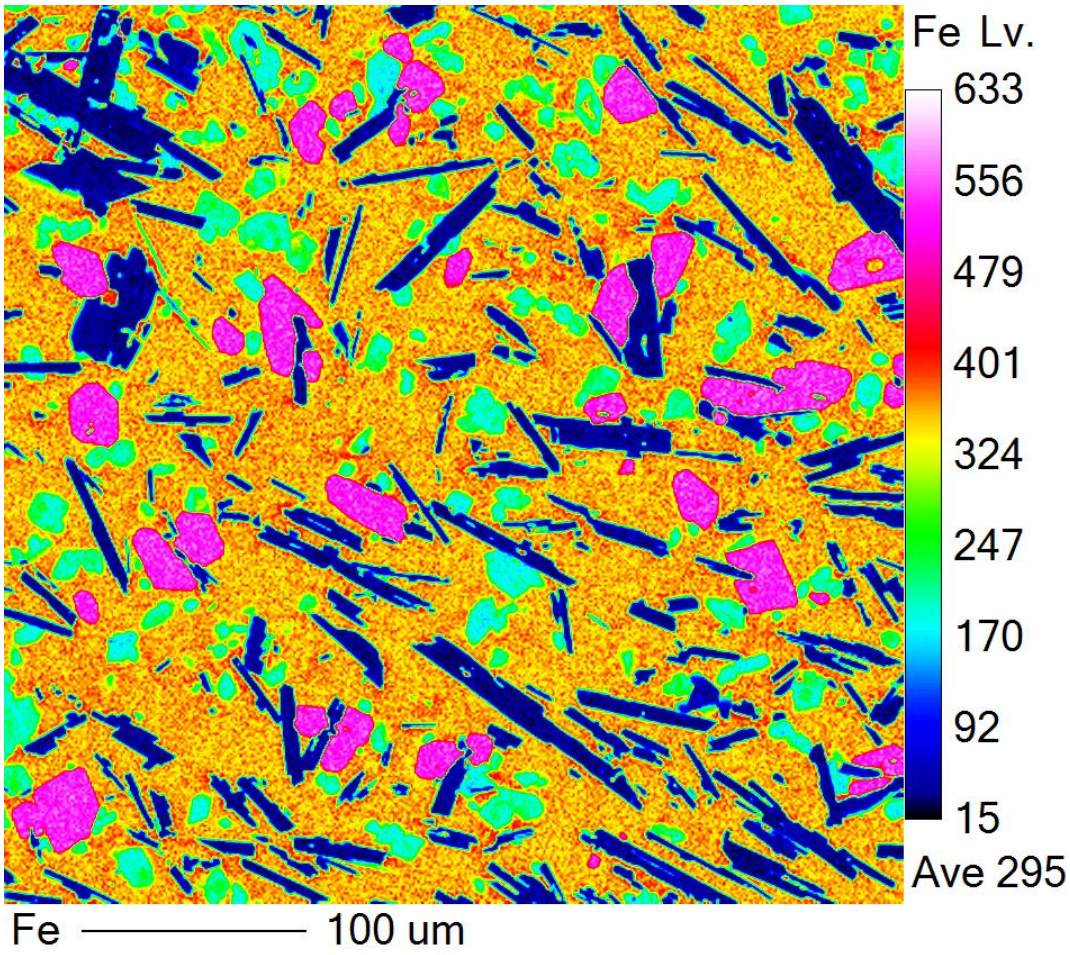

Fe map of 2021 lava groundmass. In the order of increasing Fe-content: blue-plagioclase, yellow-silicate glass, green-clinopyroxene, pink-olivine.

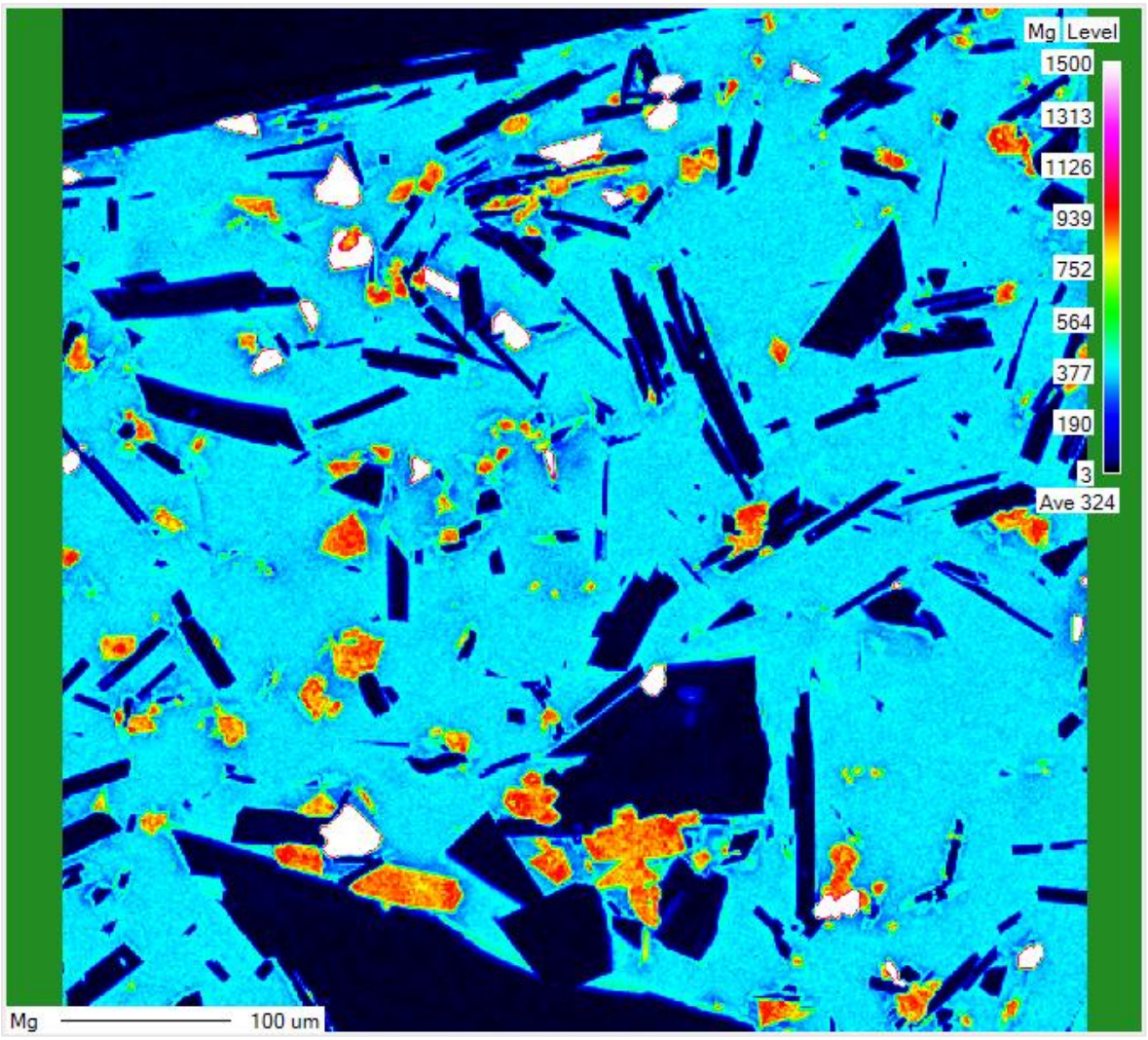

Mg map of 2022 lava groundmass. In the order of increasing Mg-content: black-plagioclase, blue-silicate glass, red-green-clinopyroxene, white-olivine. Note the heterogeneity of glass compositions close to microlites.

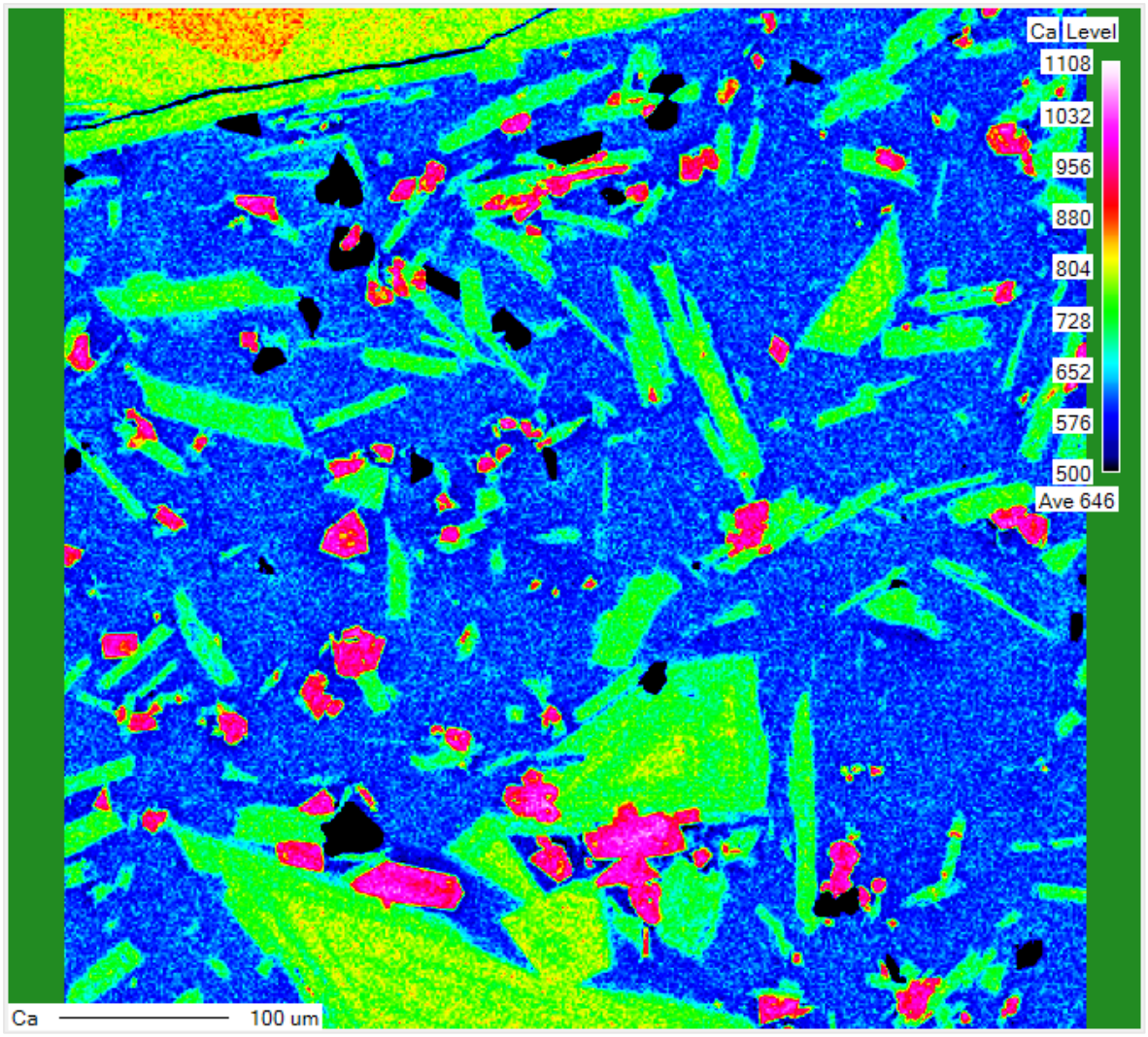

Ca map of 2022 lava groundmass. In the order of increasing Ca-content: black-olivine, blue-silicate glass, green-plagioclase, pink-clinopyroxene, red-plagioclase core.

Appendix C

Additional BSE images.

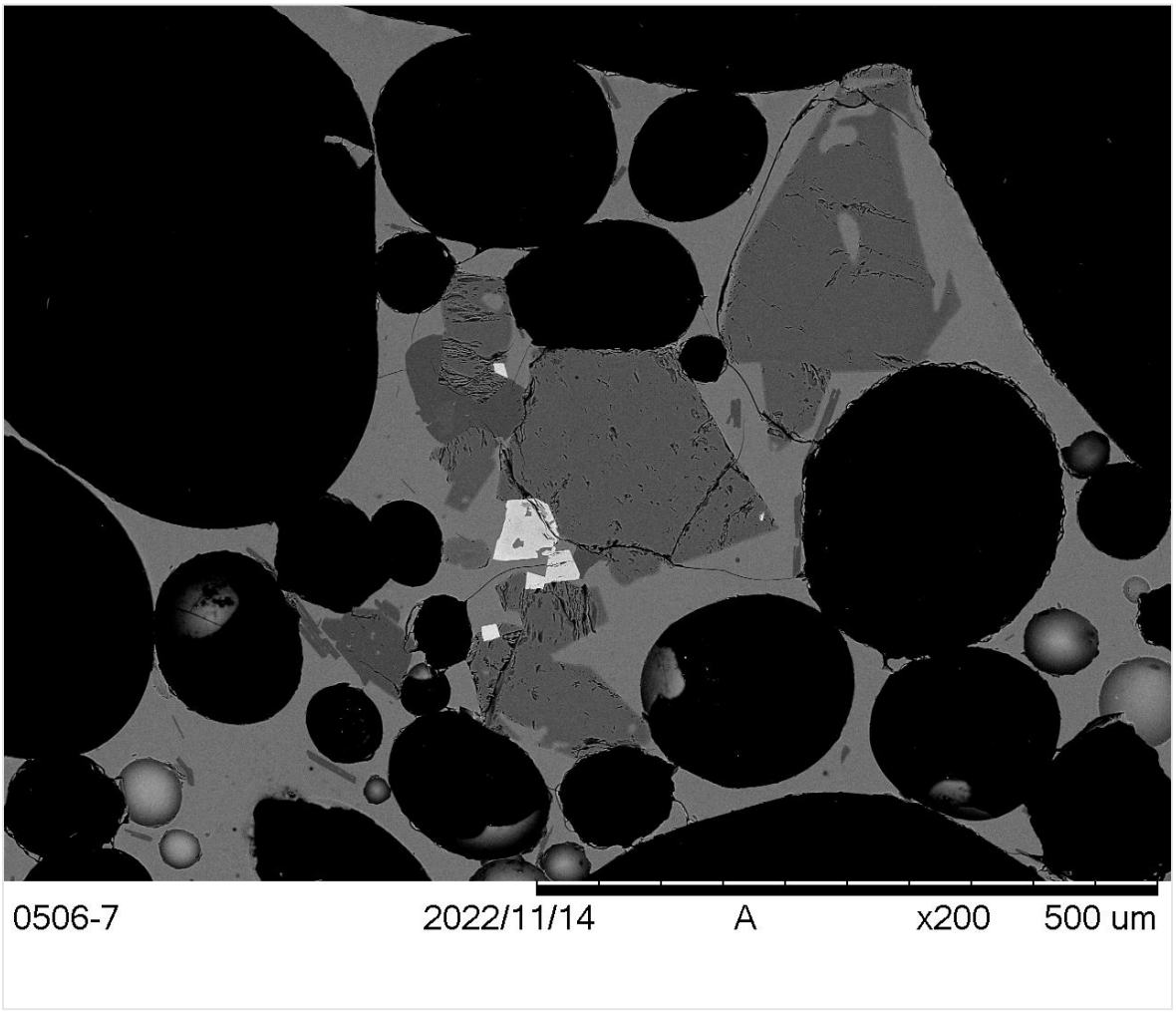

2021 tephra sample with olivine, plagioclase, clinopyroxene and Cr-spinel glomerocrysts.

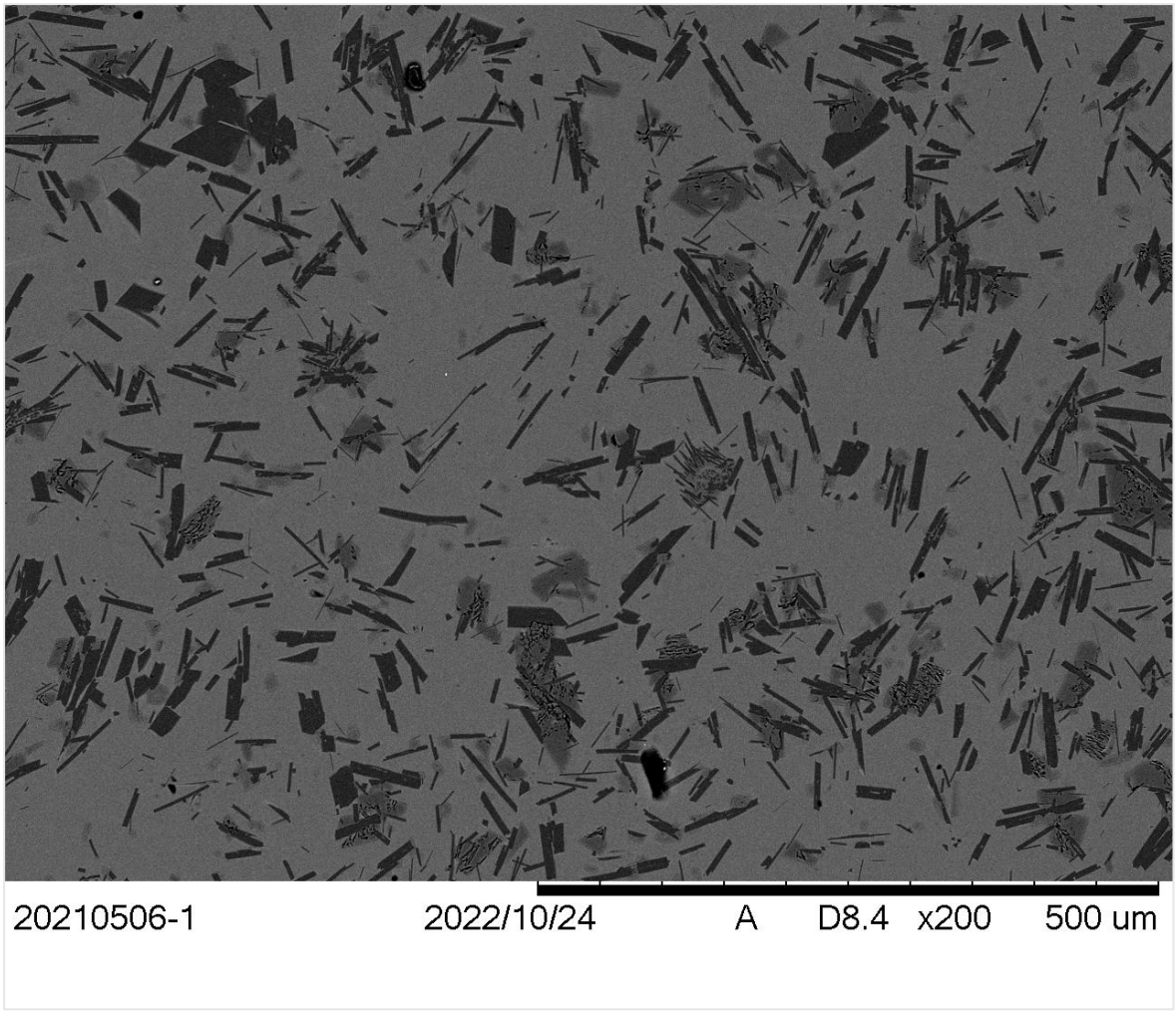

2021 naturally cooled lava sample with olivine+plagioclase+clinopyroxene glomerocrysts.

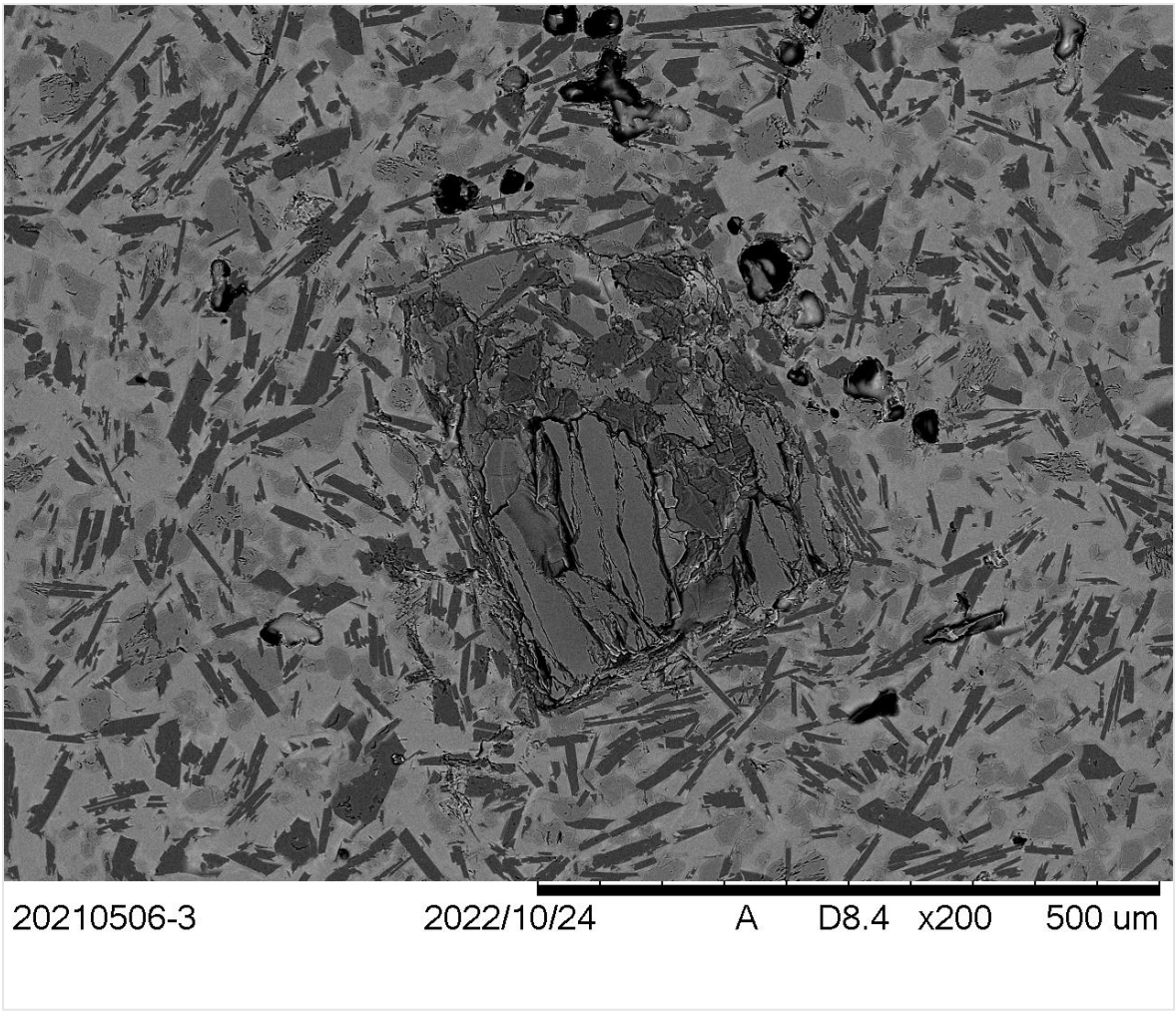

2021 quenched lava sample, with a large olivine+plagioclase glomerocryst and very high groundmass crystallinity.

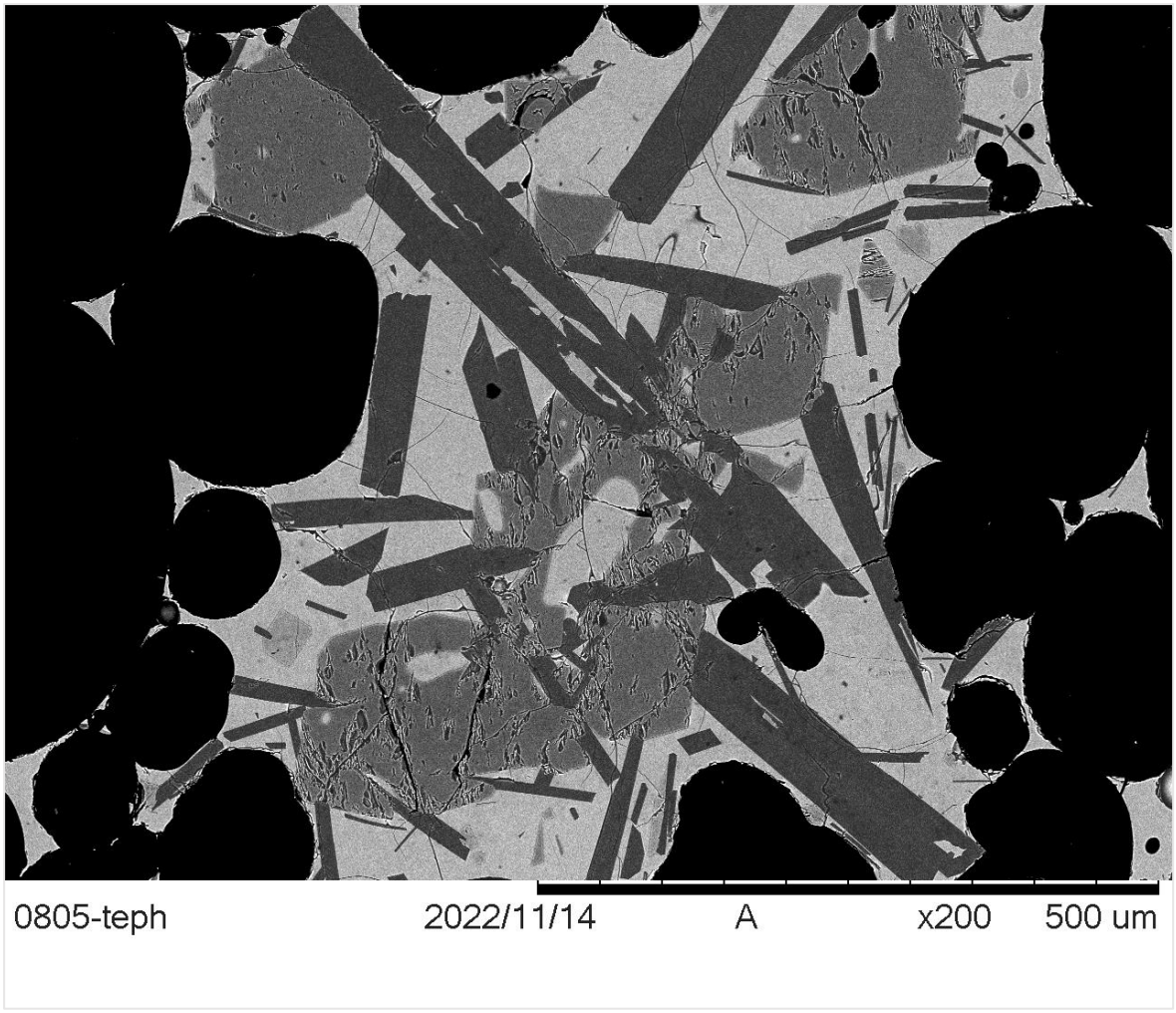

2022 tephra sample with glomerocryst of olivine+plagioclase.

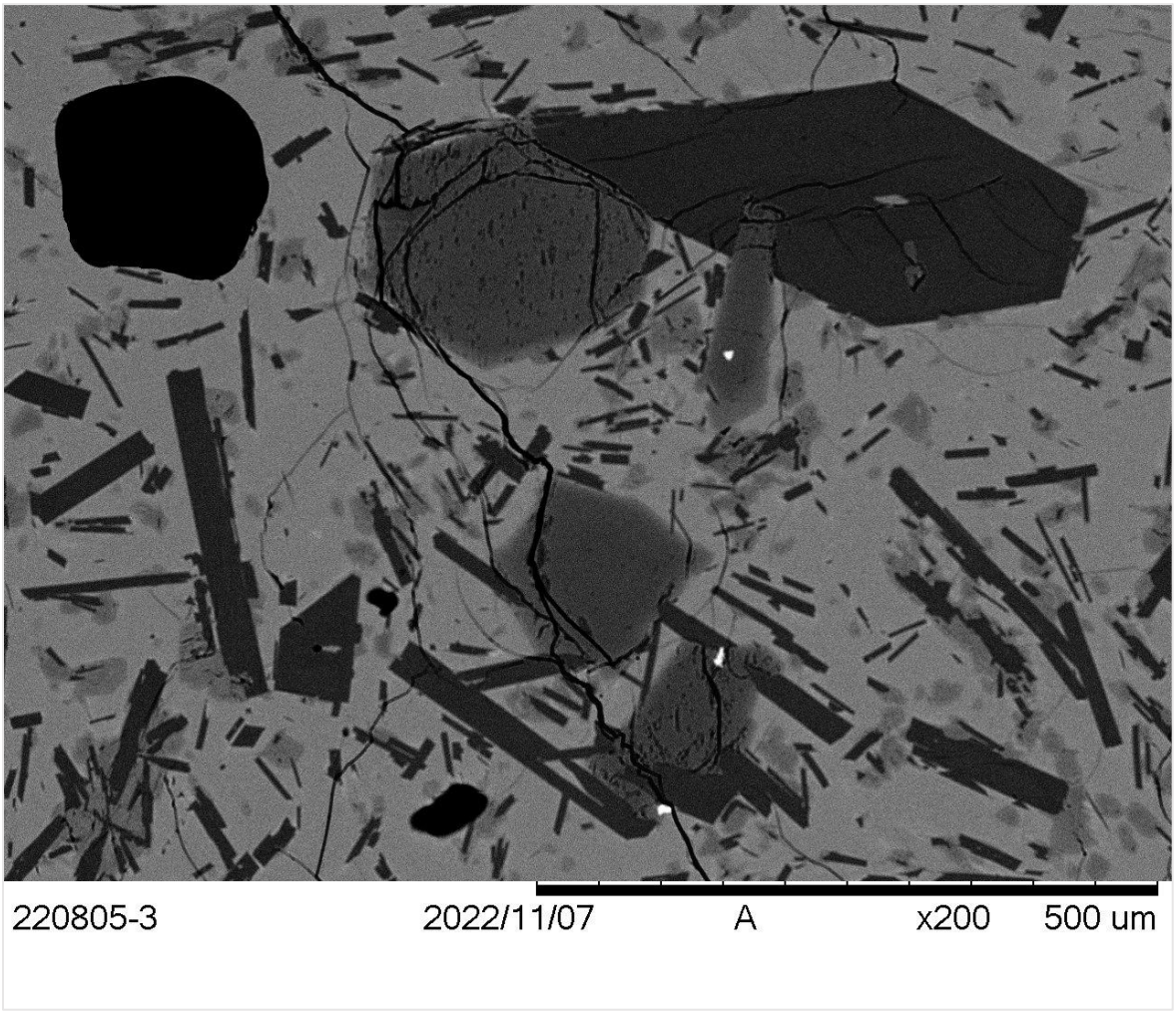

2022 quenched lava sample with glomerocryst of olivine+plagioclase. Note the normal zonation of olivine microphenocrysts and the bright iclusions of Cr-spinels.

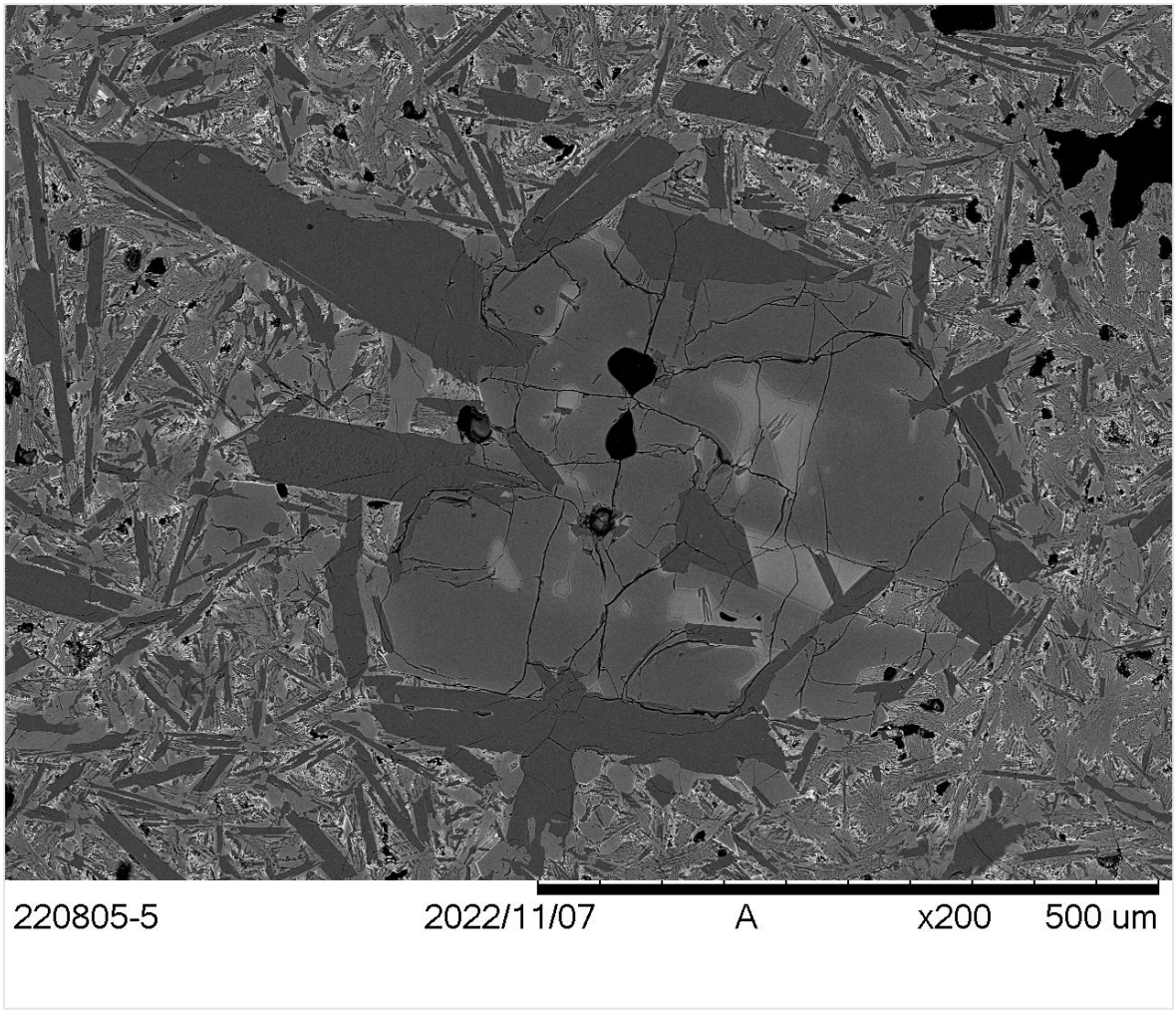

2022 naturally cooled lava sample with glomerocryst of olivine+plagioclase. Note the groundmass here being holocrystalline. Silicate glass is visible only in inclusions.